November 2014

Structural Geometry and Gravity Constraints on the Palos Verdes and Cabrillo Faults

Yeliz Cengelcik
Florida State University

FLORIDA STATE UNIVERSITY

COLLEGE OF ARTS AND SCIENCES

STRUCTURAL GEOMETRY AND GRAVITY CONSTRAINTS ON THE PALOS VERDES AND CABRILLO FAULTS

By

YELIZ CENGELCIK

A Thesis submitted to the
Department of Earth, Ocean, and Atmospheric Science
in partial fulfillment of the
requirements for the degree of
Master of Science

Degree Awarded:
Fall Semester, 2014

Yeliz Cengelcik defended this thesis on November 13, 2014.
The members of the supervisory committee were:

David W. Farris
Professor Directing Thesis

James F. Tull
Committee Member

Stephen Kish
Committee Member

The Graduate School has verified and approved the above-named committee members, and certifies that the thesis has been approved in accordance with university requirements.

To all my family

ACKNOWLEDGMENTS

A heartfelt “Thank you" is in order here for all of the suggestions, supports and encouragements that have been so liberally provided through this master project. I appreciate a lot your supports and guidance for successfully completing this work. No doubt without them, I never have been able to finish my thesis.

In the first place I would like to thank to my advisor Dr. David Farris for his help and support to me during my master years. His patience and guidance definitely encouraged me a lot through this project. I am very grateful to him for the basic concept of my thesis, many hours of personal instruction in the use of the GRASS GIS and GRAVMAG programs, accompanying me to my field work for my thesis project, and helping me to give a poster presentation at GSA 2013-2014 annual meetings. I could say in the world of geosciences I have learned lots of basic stuff under his help and teaching to me. These main points helped me a lot to develop myself under the roof of geology. I always find myself lucky to have studied and completed a thesis under his guidance. I hope that one day I could be as enthusiastic, open-minded, and successful geoscientist as well as him.

Thank you to Dr. James Tull, admirable teacher, thesis committee member, and frequent encouraging mentor during this two-and half year. Thanks for suggestions on my thesis.

Thank you to Dr. Stephen Kish for being my thesis committee member. I also would like to thank him for his suggestions on my thesis.

I would like to say thanks all my friends and other teachers inside the Carraway Geology Building. Thanks a lot to Dr. Leroy Odom and Dr. Neil Lundberg for made me believe that I can reach my Master degree.

I will forever be thankful to my former college research advisor, Dr. Zakir Kanbur. He was very helpful with his suggestions and support to me for applying to master education sponsorship provided by Turkish Petroleum Corporation. Thanks to this sponsorship, I had the opportunity to come to US and develop myself. I am definitely glad that I was one of his research student when I was in college.

I will forever be grateful to Taner Tanis, for being a good intern advisor to me in Turkish Petroleum Corporation, during summer 2009. After my internship he was like a friend to me. I appreciate his true friendship and guidance in the business life. Thanks to him I am one step close to my life dreams. I am looking forward to start working in Turkish Petroleum Corporation and to be a colleague of him.

I would like to thank the Turkish Petroleum Corporation for providing me the scholarship during my graduate program in US. I know that without this, I will never be able to cover all the financials of my graduate program at FSU.

I especially thank to my mother, father, sisters, and brothers in law. My precious parents have sacrificed their life for my sisters and myself. They always tried to prepare us good for challenging life in unconditional love and care. I love all my family so much and I believe that without their love and care, I would not have made it. My sisters Fatma Ozdemir, Funda Kanat, Filiz Cinar, and Yesim Cengelcik have always been my best friends. During my life in US I was separated but I always felt like I was home with them. I also thanks my brothers in law Olcay Ozdemir, Muammer Kanat, and Ahmet Cinar for being a good brother to me too. They altogether made me believe that coming Florida State University for graduate program is precious and worth to try. Their best effort made me feel strong. I am very grateful to be a part of this family.

I would like to thank to my boyfriend Irfan Saygili for his encouragement and support not only when I was here, but also for his approval of my decision to obtain a Master degree in geology at Florida State University. His sentence "If you want, there is nothing else to stop you." always energized me. I know for myself with my family they all wished the best for me and so I dedicated my success to them.

I am very thankful to my lovely roommate Tugba Sezen. There is no words to explain her support and help during two years in Tallahassee. She was not like a roommate to me she was my whole family in Tallahassee. Our apartment "135" is the roof of our sistership. She was the only person I could ask anything without doubt. I know that when we get old, she still will be there. I am very grateful to her for always being there to help.

Needless to say, I am very grateful to my lovely friends Ekin Ozakar and Sonay Bozkurt for supporting me in every steps of my thesis and in Florida State University. I could say they after their coming in the center of my life in Tallahassee, my horizon broadened a lot in every aspect. We have experienced lots of beauty in US with them and they were all perfect experiences. I was and will be happy to be with them in all my life.

TABLE OF CONTENTS

LIST OF TABLES

LIST OF FIGURES

ABSTRACT

The thesis presents and evaluates five new gravity constrained structural cross-sections about the Palos Verdes and Cabrillo faults of southern California. They both have been active since the Miocene, however the Palos Verdes fault zone is considered to be a greater seismic hazard. Using geologic, gravity and seismic data we present new interpretations about the geometry of the Palos Verdes and Cabrillo faults.

In the San Pedro and Los Angeles Harbor region approximately 125 new gravity data were collected with a Worden gravimeter and new structural cross-sections were constructed by using data of our gravity surveying. The collected data displays a Simple Bouguer gravity anomaly high near the Cabrillo fault and northwards toward the Palos Verdes fault there is an approximately 30 mGal decrease. The Palos Verdes fault itself is characterized by an inflection in the gravity data and a relatively flat zone immediately to the north. This shelf in the gravity data is important because the highly productive Wilmington Oil Field is located in this area and it is likely a product of the particular geometry in the region. The Palos Verdes fault also forms the edge of the larger Los Angeles Basin. Our basic interpretation is that the Palos Verdes and Cabrillo faults are primarily strike slip faults. However, a horst-like block between the two faults has been uplifted and horizontally shortened. Our main interpretation is that Catalina Schist basement uplift and subsequent basin fill to the north is responsible for the large negative gravity anomalies associated with the Palos Verdes fault.

CHAPTER 1

INTRODUCTION

The introductory section will describe the main geologic and tectonic processes within the Los Angeles Basin, southern California. The review will first give the main geological history of southern California, then focus on geological details of the study area, Palos Verdes Peninsula, Los Angeles Basin in terms of the location of Cabrillo and Palos Verdes faults.

1.1 General Geology and Location of Palos Verdes Peninsula, Los Angeles Basin

The Los Angeles Basin is located at the intersection of the northwest trending Peninsular Ranges and the east-west trending Transverse Ranges and defines a deep Cenozoic basin of southern California. It is actively deforming because of the motion between the Pacific and North American Plates (Brankman and Shaw, 2009). The larger part of this plate interaction is adapted by strike-slip on the San Andreas and San Jacinto faults. Several other strike-slip, thrust, and reverse faults are leading long-term slip events across the region (Meade and Hager, 2005). The Palos Verdes Peninsula is located at the southwestern most margin of the Los Angeles Basin (Figure 1.1). It is formed by motion along the Palos Verdes and Cabrillo faults. The northern border of the Palos Verdes Peninsula is controlled by the Palos Verdes fault and represents a break in the coastal crust along where the Palos Verdes Peninsula is being uplifted. There are some components of compressional forces along the California coast with approximately slip-rate 50-55 mm/yr. and these forces are responsible for uplift and anticline formation in the Palos Verdes Region (King and Myers, 1998). A more detailed review about the geology of the Palos Verdes Peninsula and Los Angeles Basin is presented in the following section.

1.2 Brief Tectonic History

This chapter provides an introduction to the geology and tectonic settings of southern California. A basic overview about the main geological units is offered together with the chronology of the tectonic events.

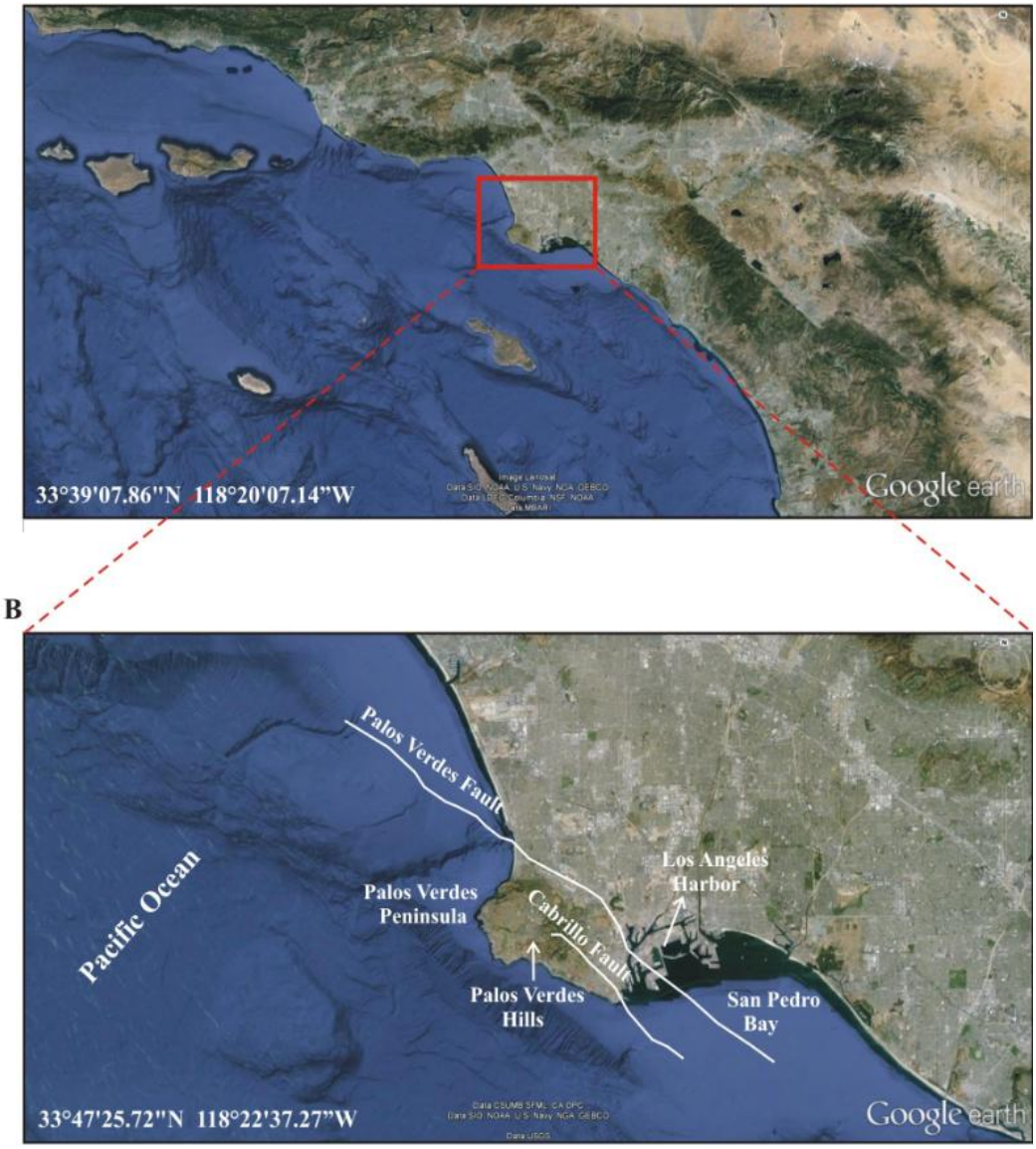

Figure 1.1 Regional location map showing Palos Verdes and Cabrillo faults in Los Angeles Basin (captured from Google Earth).

1.2.1 Origin of Modern Transform Boundary of Southern California

The oceanic Farallon Plate subducted beneath the North American throughout the Mesozoic and Tertiary geologic periods. This subduction margin dominated California tectonics during this time. Approximately 30 Ma, the western edge of the North American collided with the Pacific-Farallon Ridge. When the Pacific spreading ridge first encountered to the North American Plate at 28 Ma the convergence ended and a transform boundary began to form (Figure 1.2). Overtime, the new transform plate boundary extended in length from north to south. As the North American Plate continued its westward movement, the length of the transform boundary was extended by the process of triple junction migration.

The block diagrams on Figure 1.2 explains that how the subduction took place along the west coast of the North America 30 million years ago to the present. The westward-shifting of the North American Plate began to override the spreading ridge between the Farallon Plate and the Pacific Plate starting in 30 million years ago. This action was resulted with division of the Farallon Plate into two smaller plates, the northern Juan de Fuca Plate (JdFP) and the southern Cocos Plate (CP). The intersections between three tectonic plates, the North American Plate, the Farallon Plate, and the Pacific Plate began to move north and south along the western edge of the west coast almost 20 million years ago. The intersections between three plates are presented by triple junctions shown as red triangles in the block diagram. When the North American Plate encountered the Pacific Plate, the San Andreas transform fault system formed. The modern San Andreas transform fault system extends from the Salton Sea in the south to the Mendocino Triple Junction in the north.

In general, types of bedrock and geologic structures of southern California are represented by the displacement between the Pacific and the North American Plates. After a while the prior

geologic structures in the region formed during the Paleozoic, Mesozoic, and early Cenozoic Eras. The Mesozoic margin geometry of accretionary complex, forearc basin and arc batholith have been substantially deformed and structurally shuffled by the transition to strike-slip tectonics (Wallace, 1990).

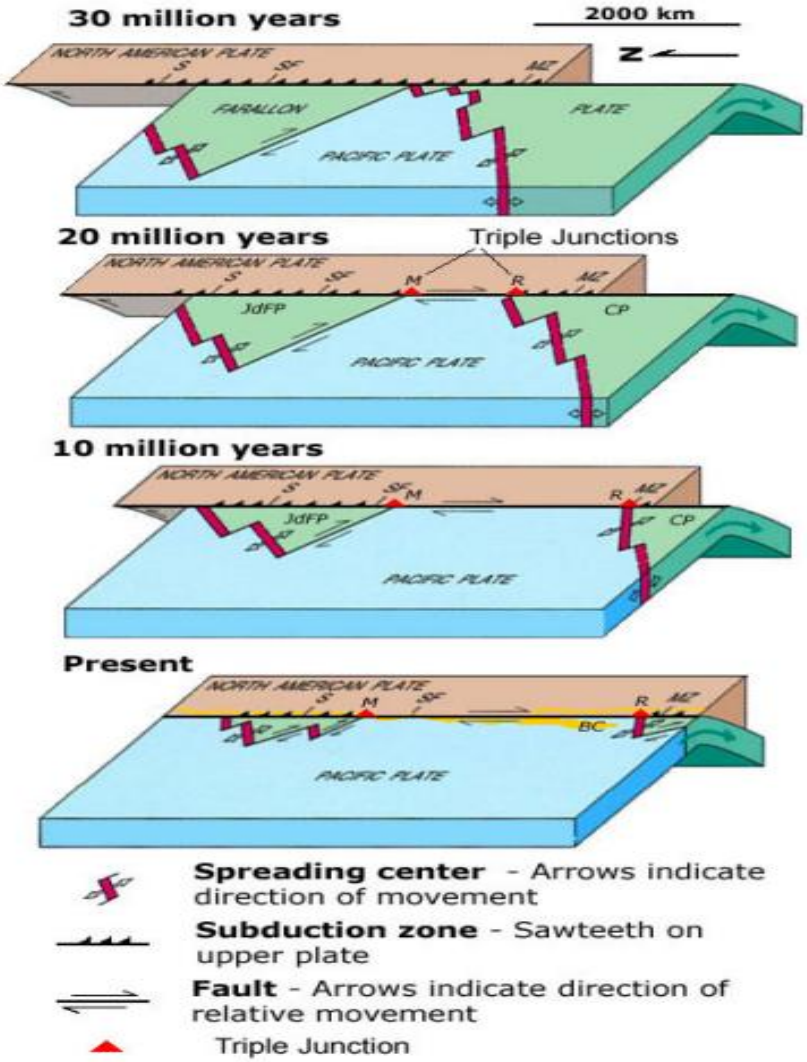

Figure 1.2 The block diagram of plate interactions between North American and Farallon Plates with the formation of the San Andreas transform fault system (modified from USGS Professional Paper 1515).

1.2.2 San Andreas Transform Fault System

The San Andreas transform fault system is complex with multiple segments (Figure 1.3). Many of them are strike-slip faults with including San Andreas transform fault itself. The geology of southern California is mostly affected from the San Andreas transform fault system since the bedrock of this area is deformed and divided into some parts by the existence of San Andreas transform fault system. The major motion of this fault system is right-lateral and it accommodates approximately 30-35 mm/yr. slip-rate between the Pacific and the North American Plate.

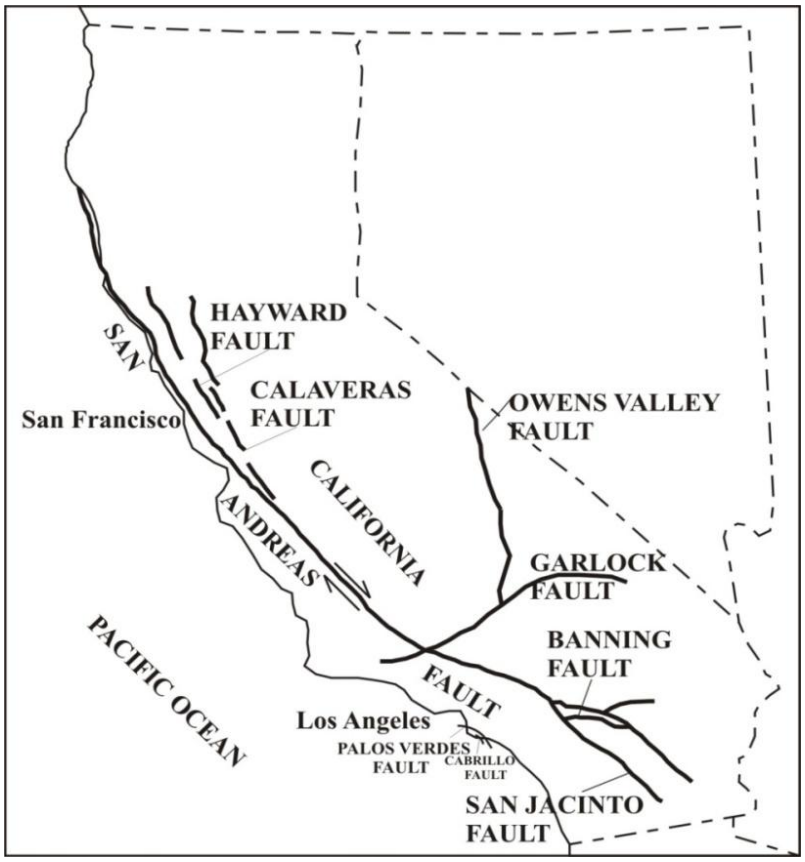

Figure 1.3 Regional map of the San Andreas and some other faults in California (modified from USGS Professional Paper 1515).

Most of the remarkable geologic settings of southern California are associated with the San Andreas transform fault system. The Big Bend in the San Andreas transform fault system, is a westward curve in the fault that creates a localized zone (~ 150 km across) of contraction. The result of such contraction is the formation of the E-W thrust fault bounded transverse ranges. This area is the most complex tectonic location in California. In this location, the San Andreas transform fault intersects the left-lateral Garlock fault, the one major east-west trending fault in southern California. The left-lateral motion on the Garlock fault is thought by some to have caused the Big Bend. The San Gabriel Mountains at the north of the Los Angeles formed as a result of the Big Bend related contraction and crustal block rotation. The San Andreas transform fault separates this mountain ranges from the San Bernardino Mountains. The southern California plate boundary is a very complex with multiple parallel strike-slip faults. The San Jacinto fault is the most seismically active fault in southern California today. Many of the hills and most of the basins in this area are related to the strike-slip fault mechanisms within the San Andreas transform fault system.

1.3 Tectonic Evaluation and Regional Structure of the Study Area

Los Angeles Basin in southern California is bounded with two major active fault systems, the northwest-trending, right-lateral strike-slip faults and the east-west faults which are mostly left-lateral or thrust faults that bound the Transverse Range (Bilodeau et al., 2007). Los Angeles Basin represents a wide zone of deformation due to its location between the Pacific Plate and North American Plate (Yerkes, 1985).

The present tectonic regime of the Los Angeles Basin is began in the Mesozoic Era. The tectonic history of this area consists of three stages since Mesozoic Era. The first stage began with the development of a continental margin subduction zone along the western edge of the North

American Plate in the Mesozoic (150-145 Ma). During this stage various Triassic-Cretaceous rocks were emplaced within the magmatic arc-trench system, either as sediments (forearc basin), granitic rocks (magmatic arc), or blueschist and greenschist metamorphic rocks (accretionary prism) (Dickinson, 1981; Wright, 1991; Crouch and Suppe, 1993; and Ingersoll, 2001; and Bilodeau et al., 2007).

The second major stage was activated by the ongoing collision between the East Pacific Rise and the subduction zone near the Los Angeles region. In this stage several subparallel right-slip faults formed since the local plate boundary was changed from subduction and oblique convergence into transform motion (Atwater and Stock, 1998). The transrotational and transtensional tectonic development of this stage was controlled by the large-scale crustal block rotation and rifting (Wright, 1991; Crouch and Suppe, 1993). Most of the sediments existing in the Los Angeles Basin were accumulated during the tectonic subsidence and transrotation of the western Transverse Ranges (Mayer, 1991; Yeats and Beall, 1991; Rumelhart and Ingersoll, 1997; and Ingersoll, 2001).

The opening of the Gulf of California and the eastward relocation of the Pacific-North American Plate boundary in southern California to its present configuration triggered the beginning of the stage three in the Miocene-Pliocene (6-4 Ma) (Wright, 1991). The San Andreas transform fault bends westward resulting in strain partitioning between the San Andreas and the north-south compressional stress regime. Major uplifting and crustal shortening along an east-west trend in southern California in the Transverse Ranges began due to the existing stress in this area. The Plio-Pleistocene transpressional deformation turned many Miocene detachment faults into low-angle thrusts (Figure 1.4) (Crouch and Suppe, 1993).

While most of the modern topographic features in Los Angeles region are characterized by these thrust systems, other Los Angeles region topographic features such as Palos Verdes Hills are formed by the transpressional strike-slip tectonic stresses (Bilodeau et al., 2007).

The basic structural interpretation of the Palos Verdes Hills is an anticline. Especially on the southwest of the Palos Verdes fault zone several anticlines and synclines are related with this zone and they trend generally 290˚-300˚, slightly oblique to overall strike of the fault zone (Brankman and Shaw, 2009).

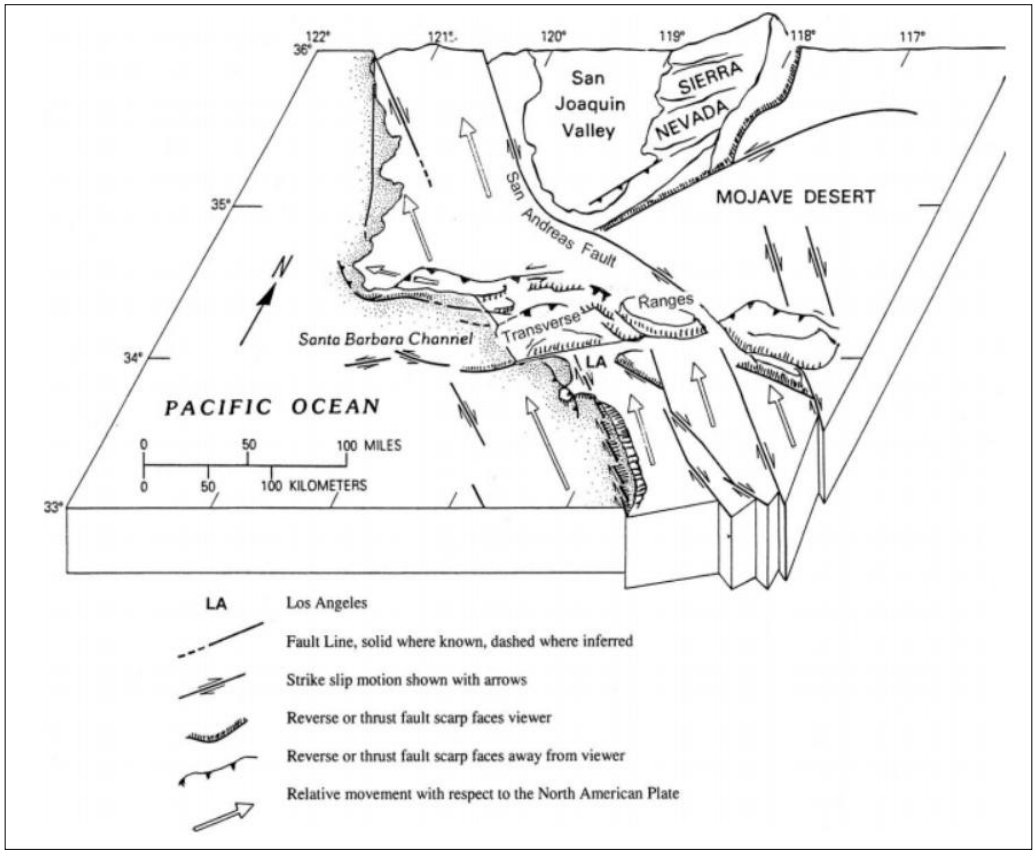

Figure 1.4 Crustal block diagram showing relative motions around Los Angeles. The view displays the Transverse Ranges bounded by reverse and thrust faults with noticeable scarps (Yerkes, 1985) (modified from Bilodeau et al., 2007).

The general structure of the San Pedro Segment of the Palos Verdes Peninsula is quite complicated; mostly consisting of anticlines and synclines. The intense transition in the region took place during the upper Pliocene, less marked deformation developed during the middle Pleistocene, and weaker deformation revealed near the end of the upper Pleistocene (Woodring et al., 1946). The markers of middle and upper Pleistocene deformation are visible only along the north border of the hills, where the lower Pleistocene strata are strongly deformed. The Palos Verdes and Cabrillo faults cut both the basement rocks and sedimentary rocks and ongoing syntectonic sedimentation is also an important geologic component in this region.

1.4 Regional Stratigraphy of the Study Area

Blueschist-and amphibolite-facies metamorphic rocks due to the past subduction of the Farallon Plate beneath the California Continental Borderland (CCB) were uplifted from lower crustal depths and exposed on the surface as the Catalina Schist. The Catalina Schist basement rocks form the crystalline basement beneath the Los Angeles Basin and are exposed in the core of the Palos Verdes Anticlines. The Schists are the oldest rocks in the Los Angeles Basin, derived from metamorphosed Franciscan basic igneous rocks (Woodring et al., 1946). Regional uplift of the Catalina Schist basement rocks took place during early the Miocene and is responsible for the absence of older sedimentary rocks beneath the inner CCB.

The basement rocks of the Los Angeles Basin and the Palos Verdes Anticlines is overlain by thick Miocene and younger sedimentary rocks. Along the northern margin of the Los Angeles Basin, the thickness of the Miocene and later deposits are approximately 914 meters (Woodring et al., 1946). The Monterey Formation, deposited uncomfortably on top of the Catalina Schist, is Miocene age. There is an increase in thickness of the Monterey Formation southward and it is

explained as outcropping of older strata by Woodring et al., 1946. The thickness of the Monterey Formation is almost 610 meter and consists of three members; the middle Miocene Altamira Shale, the upper Miocene Valmonte Diatomite, and the upper Miocene Malaga Mudstone (Woodring et al., 1946).

The Altamira Shale member includes layers of volcanic tuff and basalt intrusions. The thickest unit of the Monterey Formation is the Altamira Shale with varying thickness from ~300 m in the eastern edge of Palos Verdes Hills to ~600 m at the western end (Conrad and Ehlig, 1987). The lithofacies of this member are mainly characterized by the existence of silty shale, cherty shale, and phosphatic shale.

Overlying the Altamira Shale is the 125 m thick Valmonte Diatomite includes primarily diatomite and diatomaceous shale, deposited between 12.5 and 7 Ma ago (Rowell, 1982). On top of the Valmonte Diatomite the ~150 m thick Malaga Mudstone unit is existing (Woodring et al., 1946). This member deposited between 7-3.5 Ma ago and consists of terrigenous, micaceous and clay (Conrad and Ehlig, 1987).

While the Monterey Formation overlies the Catalina Schist basement rocks, the lower Pliocene Repetto Siltstone overlies the Monterey Formation with local disconformities. Lower Pleistocene strata appear on the north. The east borders of the Palos Verdes Hills lie conformably on the Repetto Siltstone and lap up on different parts of the Monterey Formation. Respectively; they are composed of 110-190 meter of sand, silt, and calcareous strata. The Palos Verdes Sand rests unconformably on Lower Pleistocene strata (older formations). Miocene basaltic sills intrude the lower and middle parts of the Altamira Shale member of the Monterey Formation, however the basalts are not known to occur in younger strata (Woodring et al., 1946). All these explained

units are presented in the "Geologic map of Palos Verdes Peninsula and Its Vicinity" (Dibblee, 1999) (Figure 1.5).

1.4.1 Surficial Sediments

On the map surficial sediments are mainly represented by "Qs". "Af on Os" defines the artificial fill around the harbor area and "Qoa" represents the rocks older than "Os" type surficial sediments while "Ols" representing landslide debris. All these type of surficial sediments are beach sediments ranging from sand to cobble-boulder gravel. Woodring et al. (1946) described these sediments as older alluvium and non-marine terrace cover. He pointed out that they are sandy loam and loamy clay with including sand and pebble gravel in Palos Verdes Hills.

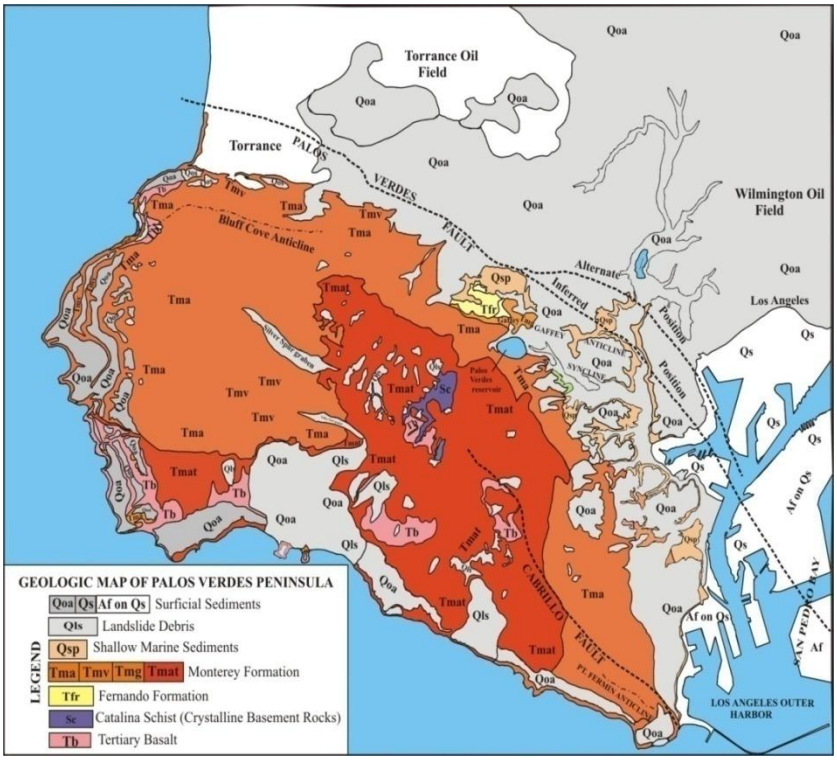

Figure 1.5 Geologic map of Palos Verdes Peninsula (modified from "Geologic Map of the Palos Verdes Peninsula and Its Vicinity" Dibblee, 1999). (Units on the geologic map are explained in paragraphs).

1.4.2 Shallow Marine Sediments

Shallow marine sediments are weakly indurated non-marine clastic sediments. They contain abundant marine fossils. On the map they are represented by "Qsp".

1.4.3 Monterey Formation

They are Miocene deposits and rest directly on the Catalina Schist basement rocks. In the Palos Verdes Hills the Miocene strata is assigned to the Monterey Shale that is divided into three members; Altamira Shale, Valmonte Diatomite, and Malaga Mudstone.

1.4.3.1 Altamira Shale

Lower section of the Altamira Shale is represented by "Tma". This part includes mostly light-gray shale and mudstone, with tuffaceous and dolomitic strata throughout. The total thickness of this part is up to 275 m at top and contains white, fine-grained, semi-indurated tuff bed.

1.4.3.2 Valmonte Diatomite

This is the middle units of the Monterey Formation. The major lithologic components of this unit are diatomite, diatomaceous shale, and diatomaceous mudstone. Also, the minor lithologic components of this unit are mudstone, phosphatic shale, limestone, black chert, cherty shale, and volcanic ashes. They are represented by "Tmv" and the thickness of them is up to 125 m.

1.4.3.3 Malaga Mudstone

The top unit of the Monterey Formation is the Malaga Mudstone member. It consists of deep marine clastic sediments; light-gray sandstone and dark-gray-brown mudstone with diatomaceous strata and limestone concentrations. This unit is represented by "Tmg".

1.4.4 Fernando Formation

Fernando Formation consists of deep marine clastic sediments in Pliocene age and consists of soft-gray siltstone-claystone. This formation is represented by "Tfr" on the map.

1.4.5 Crystalline Basement Rocks Catalina Schist

According to the previous studies crystalline basement rocks are described as Former Franciscan basement rocks (Woodring et al., 1946). The Catalina Schist defines the basement rocks of the Palos Verdes Peninsula and are metamorphosed under subduction conditions of high- pressure and low-temperature. The Catalina Schist basement rocks consists of quartz-sericite-schist, quartz-chlorite-schist, and glaucophane-schist.

1.5 Focus on the Cabrillo and the Palos Verdes Faults

The movement between the Pacific and the North American Plates causes active deformation in the Los Angeles Basin. Approximately 35 mm/yr. out of 50-55 mm/yr. of this plate motion are accommodated by strike-slip on the San Andreas fault (Walls et al., 1998; Argus et al., 1999). Regionally the San Andreas fault is the dominant tectonic feature, however other strike-slip, thrust, and reverse faults contribute to the long-term slip budget across the region (Walls et al., 1998). These faults cut the Los Angeles region and cause major earthquake hazards due to their close proximity to metropolitan Los Angeles and other urbanized areas (Fisher et al., 2004). The Palos Verdes fault zone is one of three major fault zones (Newport Inglewood fault, Santa Monica fault, and Palos Verdes fault) located within urbanized Los Angeles (Wright, 1991). The Palos Verdes fault has a complex fault geometry and slip patterns. These components suggests that the Palos Verdes fault may contribute M_W 6.6-6.9 earthquakes for single-segment rupture and M_W 7.1-7.3 multisegment ruptures (Brankman and Shaw, 2009). The average slip-rate of

Palos Verdes fault is 3.0-3.7 mm/yr.. The slip-rate of the Cabrillo fault is expected as <1 mm/yr. both on offshore and onshore (Baher et al., 2005).

This study mainly focuses on structural constraints of the Palos Verdes and Cabrillo faults.

1.5.1 Palos Verdes Fault

The Palos Verdes fault is located between Los Angeles Basin and the Inner Continental Borderlands. It acts as a boundary between these two. The western edge of Los Angeles Basin involves the Palos Verdes fault (PVF) (Figure 1.6) (Brankman and Shaw, 2009). The PVF trends from northern Santa Monica Bay across to the Palos Verdes Peninsula to offshore beneath the San Pedro shelf. The length of the PVF is approximately 110 km (Clarke et al., 1985).

Palos Verdes Hills have been uplifted and shaped as active anticlines since the Pleistocene. The PVF bounds the uplifted Palos Verdes Hills to the northeast (Figure 1.7) (Woodring et al., 1946). The fault consists of several segments that together form a complex fault zone with subparallel and vertical fault segments up to 2 km wide (Fischer et al., 1987; Wright, 1991; McNeilan et al., 1996; Fisher et al., 2004). The sense of the PVF near the Palos Verdes Hills is reverse and strike-slip (Fischer et al., 1987).

Onshore the PVF is mapped by many researchers; however, the exact trace of it is unclear due to the Quaternary sediments and urbanization. Particularly northeast of the Palos Verdes Peninsula, near Los Angeles Harbor the exact location of the PVF is not clear (Stephenson et al., 1995). Also there is not enough active seismic sources in the offshore area to delineate the PVF's geometry; therefore, multiple geometries have been proposed for this fault system. Significant late Quaternary deformation took place across Santa Monica shelf and is explained as being related to the geometry about the northern extension of the PVF (Brankman and Shaw, 2009).

Further north it exhibits compressional folding above southwest-dipping faults (Brankman and Shaw, 2009).

During a period of Miocene regional extension the PVF was initially formed as a normal fault. (Brankman and Shaw, 2009). Across the fault zone, up to 1800 m vertical separation occurred on (basement) Lower Cretaceous Catalina Schist (Fisher et al., 1987; Wright, 1991). Originally the PVF was formed as a Miocene normal fault and later Plio-Pleistocene transpression caused reactivation on the PVF and turned it into right lateral reverse fault. As a result, during Plio-Pleistocene transpression small segments connected together. Subsequent interactions on small segments, the active Palos Verdes fault zone is formed (Brankman and Shaw, 2009). Overall, the PVF is mainly comprised of three fault segments (Figure 1.8). The northern Santa Monica Bay segment, the central San Pedro segment, and the southern Lausen Knoll segment.

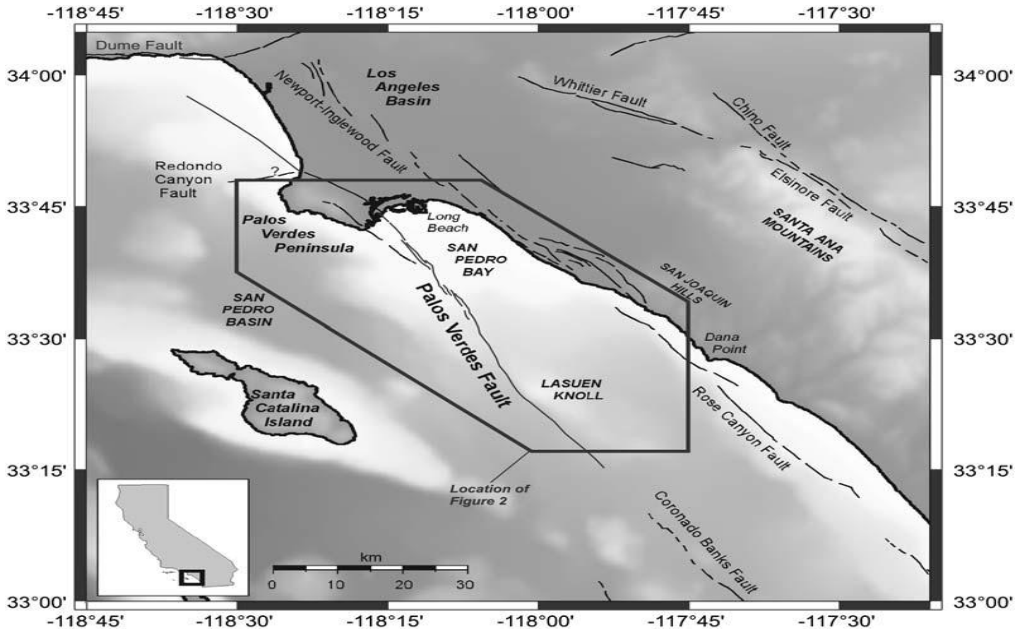

Figure 1.6 Regional location map of the Palos Verdes fault (modified from Brankman and Shaw, 2009).

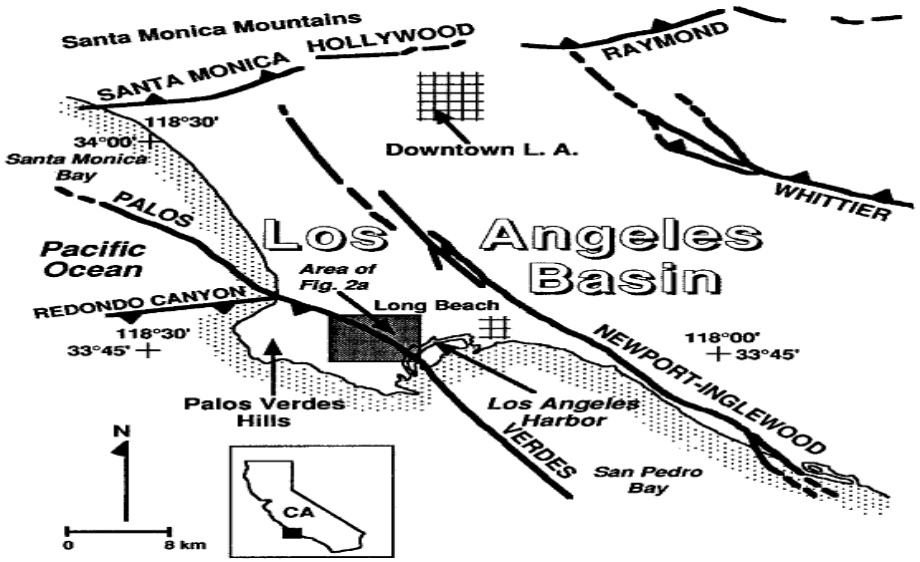

Figure1.7 Regional location map of the Palos Verdes fault in the Los Angeles Basin (modified from Woodring et al., 1946).

1.5.1.1 Santa Monica Bay Segment of the Palos Verdes Fault

As previously mentioned the length of the PVF north of the Palos Verdes Peninsula into the Santa Monica Bay is not well constrained. This segment reveals dips through southwest and active contractional folding occurs above it. Therefore some other structural deformations took place on this segment. The geometry in terms of the extension of this segment is not well defined. There is some ongoing controversy about the geometry of this segment of the PVF and two models have been pointed out to answer this controversy. One model suggests that the PVF merges with the Redondo Canyon fault and moves over it (Nardin and Henyey, 1978; Fisher et al., 1987; Wright, 1991). However, there is no evidence about extension of the active PVF north of the Palos Verdes Peninsula (Fisher et al., 2003). Alternately, other studies have documented

active deformation across Santa Monica shelf and suggest it represents the northern portion of the PVF (Figure 1.8) (Brankman and Shaw, 2009).

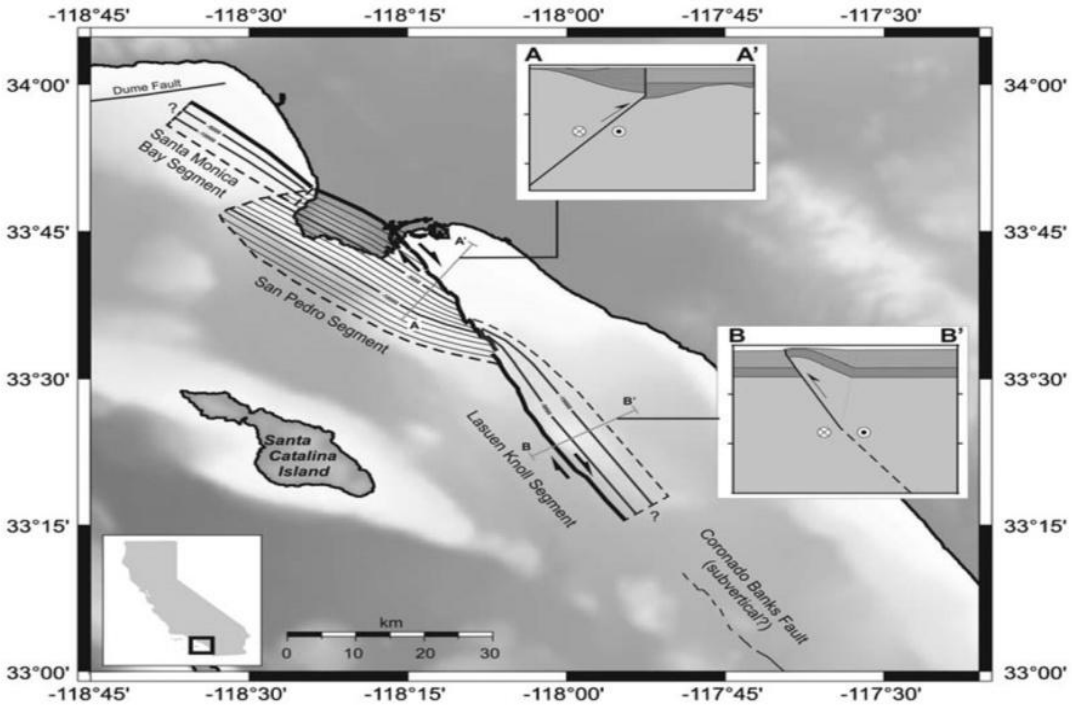

Figure 1.8 Regional location map of the Palos Verdes fault with three different fault segments (modified from Brankman and Shaw, 2009).

Further north in the Santa Monica Bay, several studies have indicated active contractional folding above southwest-dipping fault segments (Larson, 2000; Sorlien et al., 2006). If these structural assumptions are correct and represent the northern segment of the PVF, their displacement patterns and relations with the Redondo Canyon fault indicates that the Santa Monica Bay segment represents the northern segment of the PVF (Brankman and Shaw, 2009). In this segment of the PVF Miocene extension is illustrated by stratigraphic growth of units, deposited during west-down normal faulting. This portion of the PVF has most obvious vertical

displacement and dips 55° SW down to 200 m. After, these units were affected by Plio Pleistocene transpression (Brankman and Shaw, 2009).

1.5.1.2 San Pedro Segment of the Palos Verdes Fault

Woodring et al. (1946) recognized that the eastern part of the Palos Verdes Hill is covered by the onshore segment of the PVF. However, the surface expression of this portion is not well exposed because of being covered by colluvium and Quaternary landslides. Yerkes et al. (1965) named the PVF as a southwest-dipping reverse fault and builds the eastern edge of the Palos Verdes anticlines. Ward and Valensise (1994) found that a steeply southwest-dipping oblique-reverse fault explained the uplifting history in the peninsula and restraining bend geometry constructed between strike-slip fault segments in the San Pedro and Santa Monica Bays. Stephenson et al. (1995) imaged shallow fault by using high-frequency seismic profiles and came up with the idea that the PVF is a composite fault zone including several parallel, steeply dipping to vertical fault segments. Brankman and Shaw (2009) mapped the San Pedro Bay and they stated that in general similar structural correlations dominate south of the peninsula and that the fault in San Pedro Bay of the PVF representing a segment of the PVF (Figure 1.8). The Palos Verdes anticlinorium submerges southward into San Pedro Bay. The Palos Verdes Anticline is one of a series of an echelon folds west of the PVF (Brankman and Shaw, 2009).

There are two different structural domain separated by the PVF zone in San Pedro Bay (Figure 1.9). The northeast of the PVF is represented by a thick sequence of nearly flat-lying, undeformed sediments. Here continuous reflectors are corresponding to late-Miocene through Pliocene sediments of the Monterey and Repetto Formations, the late Pliocene through Pleistocene Pico Formation, and overlying late Pleistocene, Holocene, and Recent sediments.

This layer lying over the Mesozoic crystalline basement rocks (Catalina Schist) (Woodring et al., 1946).

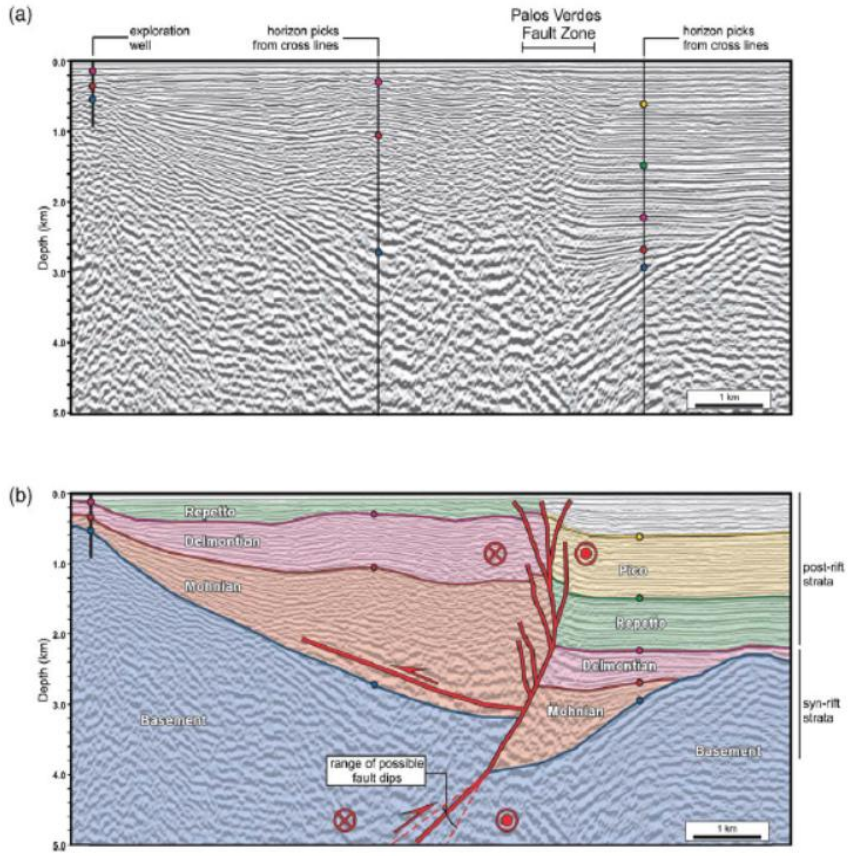

Figure 1.9 The diagram shows uninterpreted and interpreted seismic line across the San Pedro segment of the PVF. (The view indicates the structural differences between east-west side of it) (modified from Brankman and Shaw, 2009).

Conversely, the structural and stratigraphic features west of the fault are quite different than those east of it. The Miocene and Pliocene Monterey, Repetto, and undestroyed pieces of the overlying Pico formations are uplifted. Then they are deformed under the effect of contractional foldings at this area (Brankman and Shaw, 2009).

Brankman and Shaw (2009) interpreted that the normal displacement occurred at the San Pedro Bay segment of the PVF during deposition of Miocene deposition. The Miocene growth section is thicker on the west side of the PVF. In addition it is structurally higher than the indicated units on the east side of the PVF and these structural relationship shows that the PVF was structurally inverted after normal faulting. In conclusion, this segment of the fault originated in the Miocene as a normal fault, then reactivated as a right-lateral reverse fault (Brankman and Shaw, 2009).

1.5.1.3 Lausen Knoll Segment of the Palos Verdes Fault

The Lausen Knoll segment of the PVF extends almost 40 km along strike and south of the San Pedro Bay segment. The PVF is imaged as a near vertical-zone of reflectors with irregular discontinuous fault splays observable in the seismic data (Figure 1.10) (Brankman and Shaw, 2009). East of the PVF, the stratigraphy is represented with the same units as in the north. At this segment flat-extending Miocene through Quaternary strata uncomfortably overlies crystalline basement. Alternately, characteristics of the fault and associated structures in the Lausen Knoll differs with those existing on the north (Brankman and Shaw, 2009). On the Lausen Knoll segment of the PVF there is no major observed thickness changes in either the hanging wall or footwall units deposited within the Miocene or later. In addition; the stratigraphic units keeps their sense of separation across the fault zone by maintaining their thickness.

Brankman and Shaw (2009) stated that the origin of the Lausen Knoll segment and the San Pedro segment are different. The San Pedro segment formed first as a normal fault and then experienced normal-slip in the Miocene. However, the Lausen Knoll segment originated after the period of tectonic inversion in the late Pliocene to Pleistocene as an oblique right-lateral reverse fault.

In conclusion unlike to the northern segment, the southern Lausen Knoll segment show no evidence of Miocene extension and dips from 50° to 90°. Apparently these two fault segments represent independent fault segments that have attached to the PVF during Plio-Pleistocene transpression (Brankman and Shaw, 2009).

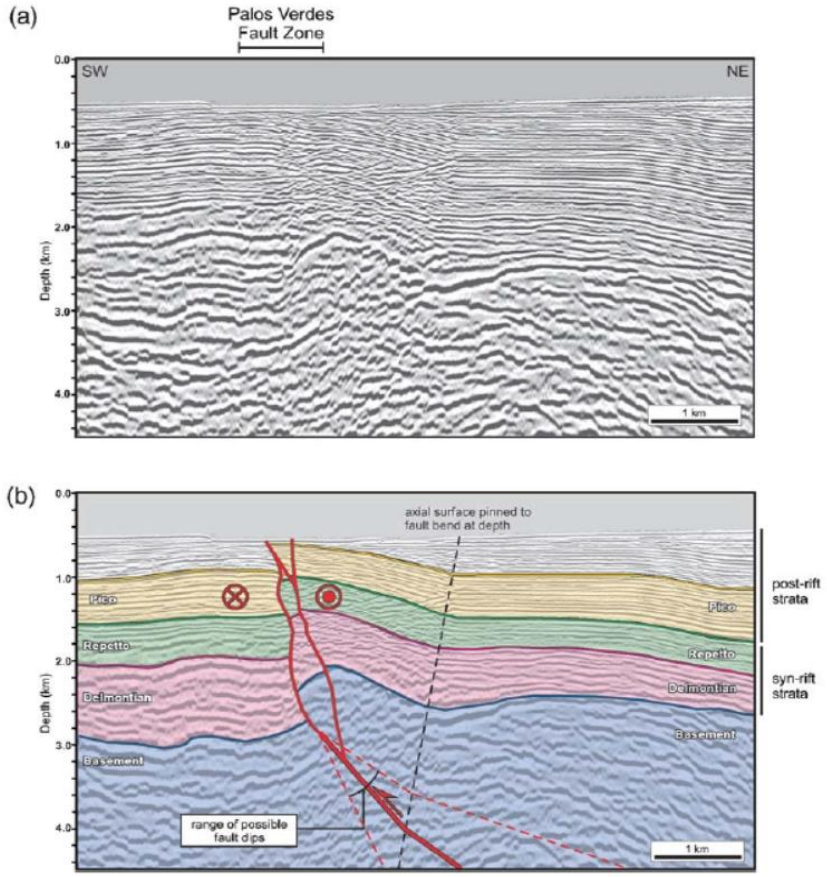

Figure 1.10 The diagram shows uninterpreted (top) and interpreted (below) seismic line across the PVF at the northern end of the Lausen Knoll segment. (The view indicates the PVF displays a steep northeast dip, with a well indicated fold east of the fault) (modified from Brankman and Shaw, 2009).

Seismicity is not concentrated along the PVF zone. Therefore researchers used different slip-rate estimations about the PVF. Stephenson et al. (1995) documented the PVF slip-rate at 2.5-3.8

mm/yr. based on the deflection of a paleochannel of the Los Angeles River, over the past 100 k.y. McNeilan et al. (1996) estimated right-lateral strike-slip rates of 2.7-3.0 mm/yr. for the near-shore portion of the PVF, based on offset of a buried early Holocene paleochannel. The uplift of the Palos Verdes Hills is controlled by right-lateral slip through a restraining bend in the PVF (Ward and Valensise, 1994). Meade and Hager (2005) estimated the slip rate is 3.4-1.4 mm/yr. on the fault. Additionally they calculated 3.1-1.5 mm/yr. uplift on a vertical PVF surface. Recently, Cooke and Marshall (2006) studied faults in the Los Angeles Basin and they concluded about 3.0 mm/yr. movement occurs on the PVF. The complex fault geometry and slip patterns of the PVF show that it is a segmented fault. It may causeM_w 6.6-6.9 earthquakes for single-segment ruptures and M_w 7.1-7.3 multi-segment ruptures (Brankman and Shaw, 2009). The PVF initially formed as a Miocene normal fault. Later Plio-Pleistocene transpression reactivated the PVF as a right-lateral reverse fault. In general it extends about 100 km from northern Santa Monica Bay to the southern Lausen Knoll (Brankman and Shaw, 2009). Movement on the Palos Verdes fault has concluded with uplift of the Palos Verdes peninsula and the Palos Verdes Hills are covered by the PVF. The PVF includes several segments that together form a complex fault zone. The three main segments of the PVF are divided into northern, central, and southern portions. According to the previous studies the average slip rate of the PVF is 2.5-3 mm/yr. (McNeilan et al., 1996).

1.5.2 Cabrillo Fault

The main characteristics of the Cabrillo fault including fault geometry and movement history are not well defined. The length of the Cabrillo fault on the onshore portion is 7.0 km and extends northwesterly from Cabrillo Beach into the central area of the Palos Verdes Peninsula (Woodring et al., 1946). On the other hand the offshore extension of the Cabrillo fault through southeast

from the Cabrillo Beach is approximately 11 km across the San Pedro Shelf to intersection with the PVF (Bryant and Raub, 1986). The Cabrillo fault transects a part of the Palos Verdes Hills (Figure 1.1) (Baher et al., 2005).

Woodring et al. (1946) indicated stratigraphic separation is in the range of 30-60 meter within bedrock at Cabrillo Beach. The stratigraphic section exposed in the hanging wall is represented by cherty and phosphatic shale from the upper part of the Altamira Shale Unit and the section exposed in the footwall is represented by siltstone from the Altamira Shale Unit of the Monterey Formation.

According to the performed seismic risk assessment of the PVFZ by Dames and Moore, and MESA between 1980 and 1983, Darrow and Fischer (1983) concluded that the Cabrillo fault cuts the Palos Verdes fault offshore, around in the middle of the San Pedro Shelf. In addition they explained that the offshore portion of the Cabrillo fault proofs of Holocene activity. So they agree with Woodring et al. (1946) as to the offshore and onshore geometry of the Cabrillo fault. At this time there was controversy about the Holocene activity along the offshore Cabrillo fault. Clarke et al., (1985) found no obvious Holocene surface separation along the offshore Cabrillo fault and they concluded that the offshore segment of the Cabrillo fault maybe a part of the Palos Verdes fault. Their work demonstrate that, despite the fact that the Cabrillo fault cuts across the seafloor, there was no obvious surface expression of it.

Dibblee (1999) prepared a geologic map of the Palos Verdes Hills. On it the Cabrillo fault extends 6.5 km from Cabrillo Beach to the northeast side of the San Pedro Hill. This map shows the Cabrillo fault as a northeast dipping normal fault.

The Cabrillo fault has a length of 10 km in the map published by Marlow et al. (2000). In this map the southwestern end of the Cabrillo fault is uncertain in terms of location and the

northwestern portion continues onshore beyond Cabrillo Beach. The calculated vertical slip rate of Cabrillo fault is 0.2 mm/yr. (Baher et al., 2005).

The expected slip rate on the Cabrillo fault is <1 mm/yr. for both the offshore and onshore segments. As indicated before, the Palos Verdes fault initiated as a Miocene normal fault (east side down), but in the Plio-Pleistocene it was reactivated as a right-lateral strike slip fault with components of reverse motion. The Cabrillo fault is thought to be related to the Palos Verdes fault and maybe a secondary structure of it (Fisher et al., 2004).

1.6 Objectives of Thesis

The purpose of this thesis is to gain better understanding of active faulting and oil production in the Los Angeles Basin. The Wilmington, Torrance and Long Beach Oil Fields are located in the Palos Verdes Peninsula and have been amongst the most productive petroleum fields in the United States with over 2,500 million barrels of oil produced (Figure 1.10). One purpose me of this thesis is to better determine the PVF geometry because the above petroleum fields located between the Palos Verdes, Huntington and Newport-Inglewood Faults. Primarily NW-SE striking right-lateral strike-slip faults are part of the North American and the Pacific Plate boundary. Fault bends and step-over structures produce structural complications that have acted as traps for petroleum.

Second purpose of this thesis is to gain a better understanding of the earthquake hazard associated with the Palos Verdes and Cabrillo faults. Shown in Table 1 the term "active" is considered to cause seismic risk in the city of Los Angeles. The Palos Verdes and Cabrillo faults are listed in the category of active faults in this table prepared by Bilodeau et al., 2007. The Palos Verdes fault is thought to produce magnitude 6.7 earthquakes and the Cabrillo fault is expected to generate magnitude 6.2 earthquake.

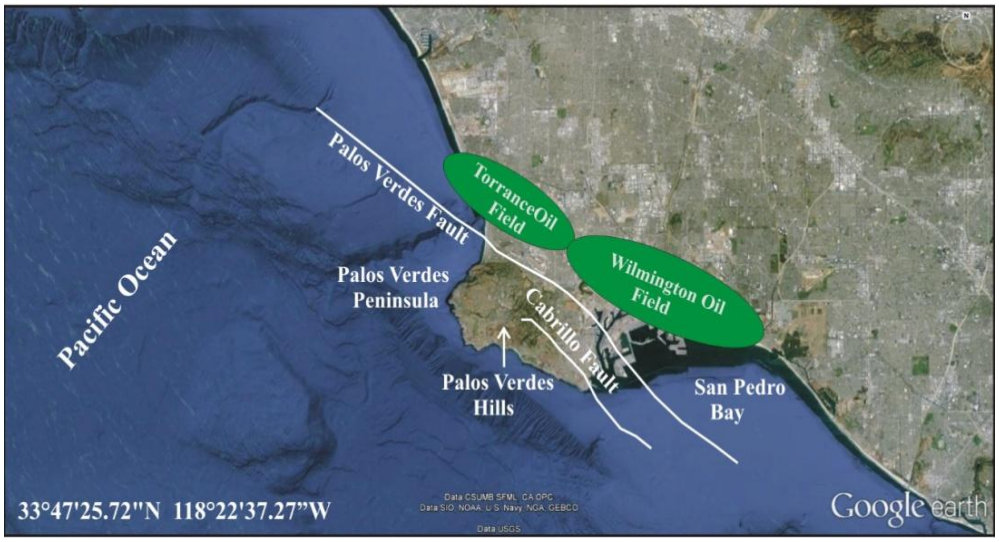

Figure 1.11 Locations of Torrance and Wilmington Oil Field on Google Earth image (captured from Google Earth).

If any rupture happens on these faults, the ground shaking will be destructive for the sitting and designing critical facilities like Ports of Los Angeles and Long Beach and for people living in the Los Angeles and Long Beach. Therefore, better understanding of the Palos Verdes and Cabrillo faults will result in improved understanding of seismic hazard perspective in the Los Angeles metropolitan region.

Table 1.1 Magnitude estimates for any rupture scenarios on the PVF segments (modified from Brankman and Shaw, 2009) (LK, Lausen Knoll segment; SMB, Santa Monica Bay segment).

Rupture Scenario	Moment Magnitude (M_W)	Recurrence Interval (yr)
San Pedro, LK, SMB	7.3	534 (497-585)
San Pedro, LK	7.2	458 (421-504)
San Pedro, SMB	7.1	399 (364-421)
San Pedro only	6.9	311 (274-325)
LK only	6.8	262 (254-306)
SMB only	6.6	181 (177-195)

Table 1.2 Late Quaternary faults in the Los Angeles Region (modified from Bilodeau et al., 2007).The term active is used in this table to infer a fault which has geologic or geomorphic evidence to show Holocene offset.(EQ=earthquake; M= magnitude)

Fault Name	Activity Status	Segment Length (km)	Segment Length (mi)	Maximum Credible EQ (M)
Cabrillo	Active	18	11	6.2
Charnock	Potentially active	>10	>6	6.2
Clamshell-Sawpit	Active	13	8	6.4
Clearwater	Potentially active	33	20	6.9
Hollywood	Active	17	11	6.4
Malibu Coast	Active	>27	>17	6.9
Mission Hills	Active	10	6	6.3
Newport-Inglewood	Active	>43	>27	6.9
North Hollywood	Active	2	1	?
Northridge	Active	15-21	9-13	6.6
Palos Verdes	Active	>77	>48	6.7
Raymond	Active	22	14	6.7
San Andreas	Active	>120	>74	8
San Antonio	Active	18	11	6.2
San Fernando	Active-potentially active	17	11	6.5
San Gabriel	Active-potentially active	130	81	>7.0
San Jose	Active	14	9	6.7
San Pedro basin	Potentially active	70	43	>7.0
Santa Felicia	Potentially active	8	5	6.1
Santa Monica	Active	>40	>25	6.7
Santa Susana	Active	28-38	17-24	6.9
Sierra Madre	Active	62	38	>7.0
Verdugo	Active	21	13	6.7
Whittier	Active	>40	>25	>7.0

CHAPTER 2

FIELD WORK DESCRIPTION AND DATA COMPILATION

2.1 Introduction of Field Work

We conducted a gravity survey using a Worden gravimeter (Figure 2.1) of the San Pedro and Los Angeles Harbor region, CA to gain a better understanding of the subsurface geometry of the Palos Verde and Cabrillo faults. Approximately 126 stations with average spacing of 300 meters were collected. Station elevations were measured with a Trimble Pro XRT differential GPS receiver and tied to absolute values using base station data from the National Geodetic Survey (San Pedro, Los Angeles, CA). Most stations have an elevation precision better than 10 cm and repeated measurements at individual stations indicate an overall precision of 0.2 mGal. Collected gravity stations in the survey area are shown on regional topographic map of the Palos Verdes Peninsula (Figure 2.2).

Figure 2.1 Worden Gravimeter and one of our Benchmark stations (located within the reddish circle)

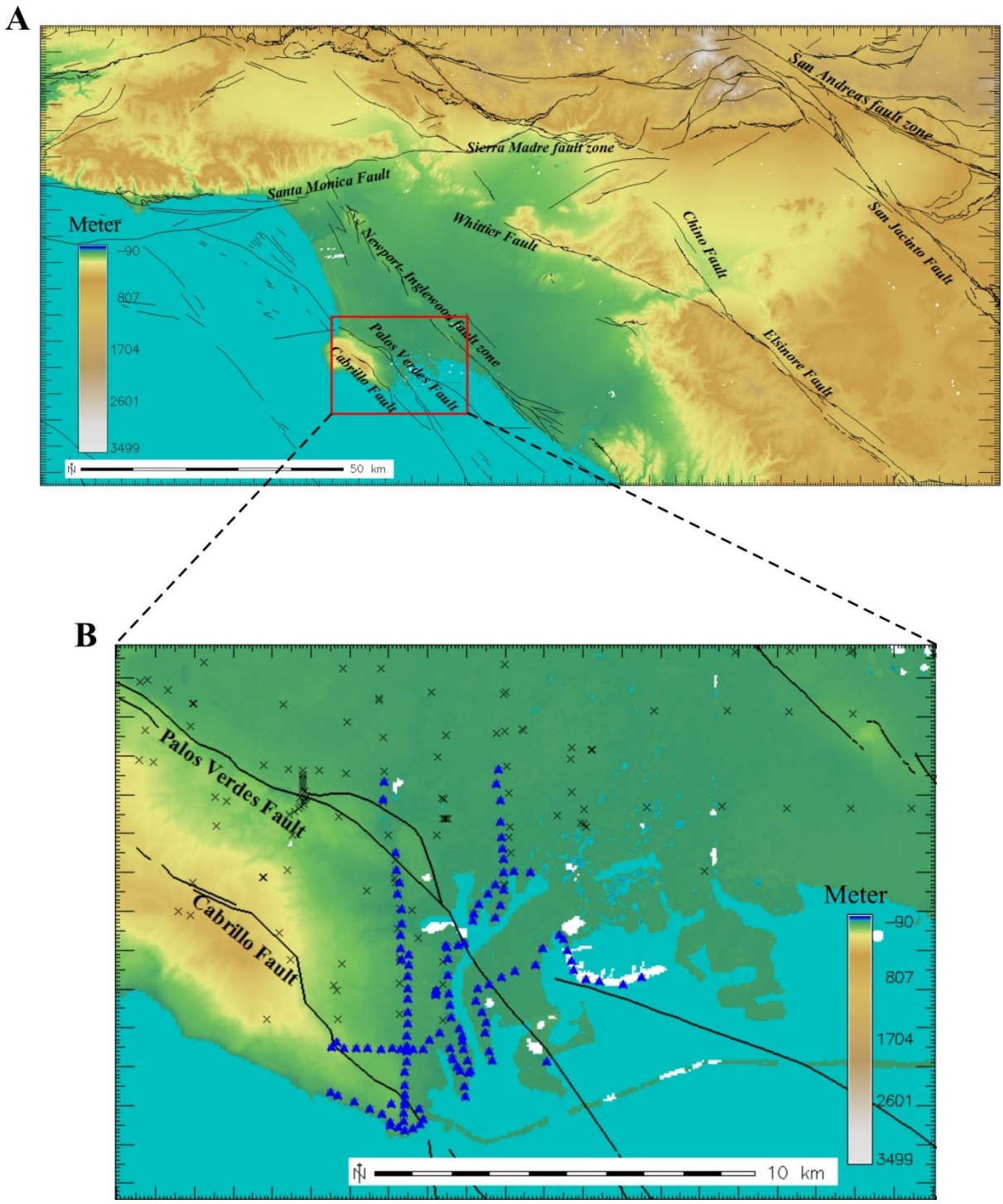

Figure 2.2 Collected gravity on Regional Topographic Map of the Palos Verdes Peninsula. A) Regional topographic Map of the Palos Verdes Peninsula and B) Extended view of the black square (Blue triangles represent gravity data from our surveying and black X's represent the data belong to previous studies).

Instrument drift, caused by small changes in the physical constants of gravimeter components, affects readings, and must be quantified for precise measurements. The easiest way to obtain a reliable reading at a selected point is to do base station readings twice in a day; at the beginning and at the end. This method averages together Earth tides and instrument drift, but limits measurement precision to approximately ± 0.2 mGal.

After all station points gathered, the data were reduced and EGM 96 was used as a vertical datum. As in many gravity surveys; we selected a density 2.67 gr/cm^3 for use in Simple Bouguer Gravity Anomaly calculation because this value is widely used in modeling and calculating elevation corrections for standardized gravity maps.

Rocks and sediment samples from survey area were collected. In the laboratory, the samples were first weighed in air and then again when completely submerged and suspended in water. The density then comes from this formula $\rho = \rho_0 W/(W - W_0)$

where W is the weight in air, W_0 is the weight in water, $W - W_0$ is the weight of the displaced water and ρ_0 is the density of water. Our measured rock density values (Appendix A) are on the low end of density values given for sedimentary rocks and overlap ranges with for unconsolidated sediments (Burger et al., 2006). However, for modeling values discussed in Chapter 3, we used average sedimentary rock density values 1.75 gr/cm^3 for sedimentary units.

Table 2.1 Density table of collected rock samples from our survey area.

Station Name	Description About the Sample	Density (g/cm^3)
13LA113A	pebbly sandstone	2.35
13LA113B	black and tan shale- siltstone	1.71
13LA113C	tan limestone	2.33
13LA113D	fine grained limestone	1.55
13LA127A	massive sandstone	1.78
13LA127B	siltstone	1.92
13LA128A	bedded siltstone, thinly laminated siltstone	1.68
13LA128B	thickly bedded siltstone	2.25
13LA128C	siltstone	2.69
13LA129	sheltered siltstone.	1.71
13LA130A	sandstone	2.6
13LA130B	siltstone	1.19
13LA130C	sandstone	2.47

2.2 Free-Air Correction

This correction handles only elevation differences between gravity station and a datum. Commonly the datum used for gravity surveys is sea level because gravity decreases 0.3086 mGal for every meter above sea level. The Free-Air correction is added to observed gravity each meter above sea level (Appendix B). The increase in height indicates an increase in distance from the Earth's center of mass and the effect is negative for stations above sea level. Unlikely, below the sea level it is subtracted since a decrease in height indicates a decrease in distance from the Earth's center of mass and the effect is positive for stations above datum (Burger et al., 2006).

2.3 Simple Bouguer Gravity Correction

The Simple Bouguer correction removes the effect of the slab between the datum and the observation point. Therefore, for observations on land, the Simple Bouguer correction has to be subtracted from the observed gravity value because it is assumed to remove any factor of the additional mass above the datum. If an observation station is below the datum, the Simple Bouguer correction must be added (Burger et al., 2006).

Since topographic masses are irregularly distributed, their effects are difficult to precisely calculate so approximation is necessary. The simplest approach assumes that topography can be represented by a flat plate extending to infinity in all directions, with a constant density and a thickness equal to the height of the gravity station above the reference surface.

At the end of our gravity survey we have reached the point where the effects of geology on the Earth’s Gravity Field can be detected. Simple Bouguer Gravity Anomaly values have already been adjusted for the effects of latitude dependent flattening and rotation, elevation, and land mass above sea level. Therefore any differences between the Simple Bouguer Gravity Anomaly

from place to place must be caused by density irregularities associated with geologic structure (Robinson and Coruh, 1988).

In our surveying we calculated the Free-Air and Simple Bouguer Gravity Anomalies.

For computational structural modeling in following chapters we used the values of Simple Bouguer Gravity Anomalies (Appendix B). Ideally, we are left with values, Simple Bouguer Gravity Anomalies that are due to density variations within the subsurface.

The Simple Bouguer Gravity Anomaly is the most commonly used technique of reducing gravity observations for exploration purposes. There are three elements of the earth model for computation of the Simple Bouguer Gravity Anomaly. The first one is latitude effect g(lat), the second is the free-air effect g(fe), and the third is the Bouguer effect g(Boug).

Then calculated gravity at a point is;

$$g(\text{calculated}) = g\ (\text{lat}) + g(\text{fe}) + g\ (\text{Boug})$$

If we name observed gravity as g (obs), the Simple Bouguer Gravity Anomaly becomes

$$g\ (\text{BA}) = g(\text{obs}) - g(\text{calculated})$$

(Observed gravity refers to an absolute gravity determination and the following corrections are applied to a dial reading of instrument in order to derive an absolute gravity value).

By using the standard Simple Bouguer reduction density value, which is 2.67 gr/cm^3 , one step of the interpolation of new data with pre-existing data is completed. In the merging process first we tried to determine what are the main differences between our new data and pre-existing data (Figure 2.3).

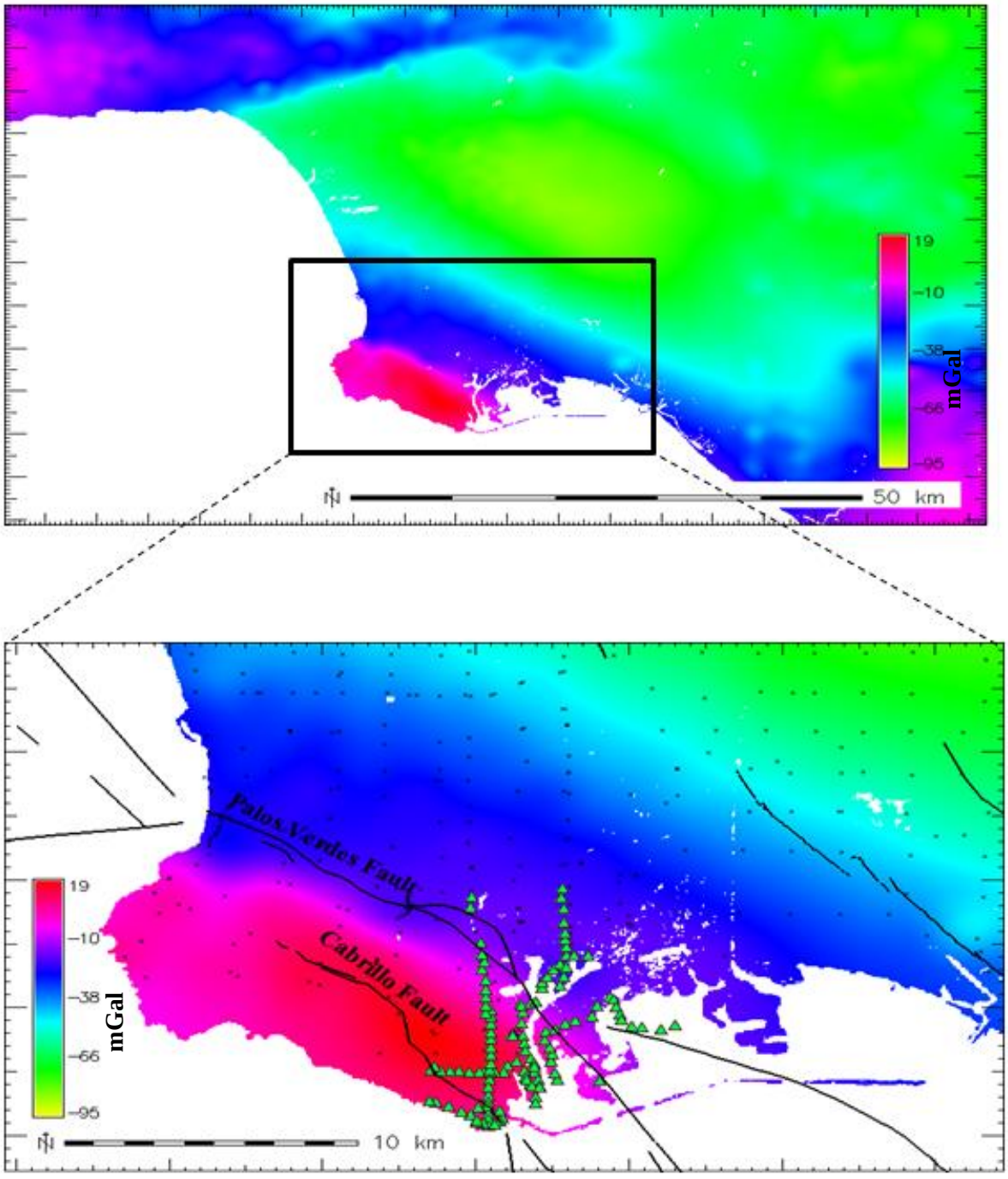

Figure2.3 Regional Bouguer Gravity Map of Southern California (Data is from the University of Texas, El Paso National Gravity database) (green triangles represent gravity data from our survey and black X's represent the data belong to previous studies).

In general our data has Simple Bouguer Anomalies 1-2 mGal lower than pre-existing data. However, our new data is 5-10 mGal higher than pre-existing data especially near the Cabrillo fault (Figure 2.4, Figure 2.5). In the next step new and preexisting data is jointly gridded by using a cubic spline procedure. At the end we were done with smooth out differences between these two data sets.

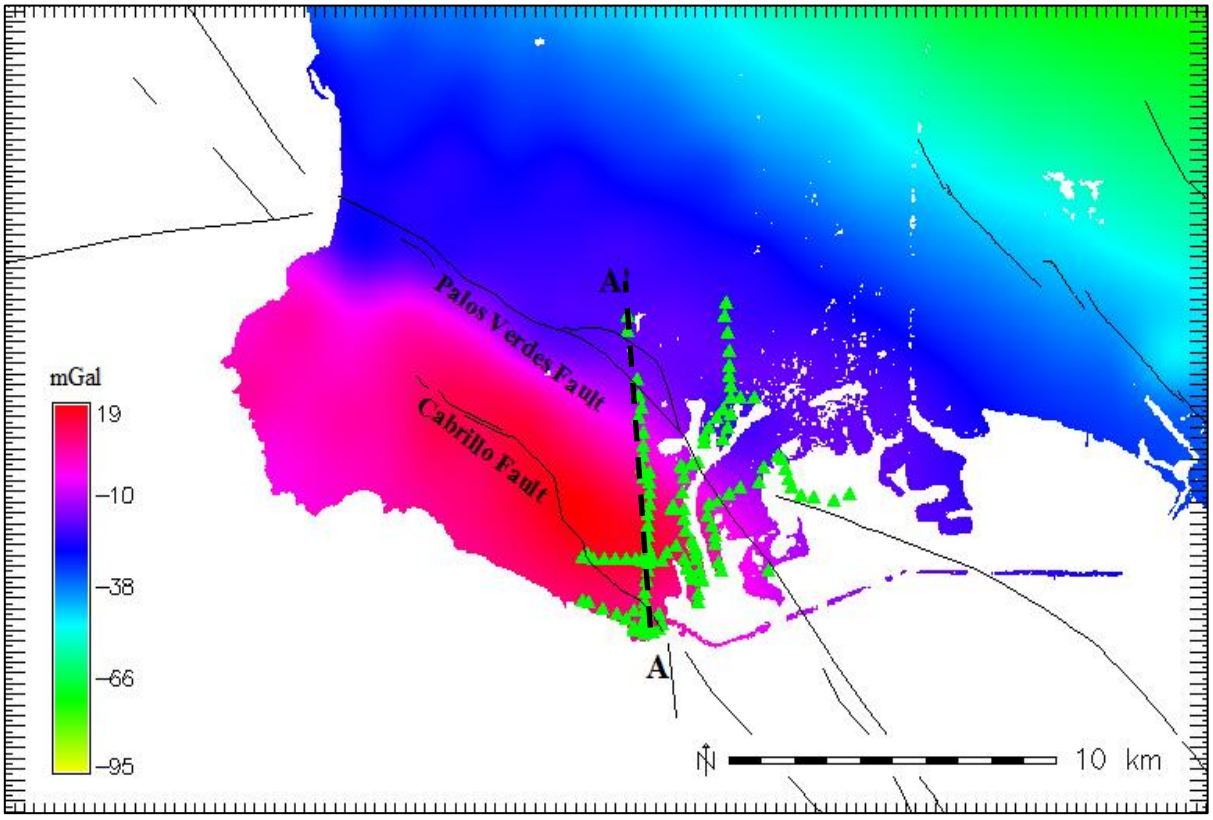

Figure 2.4 Regional Bouguer Gravity Map of the Los Angeles (built with existing gravity data set)(the A-A' profile is taken to display the differences between the newly collected gravity data set and existing data set)

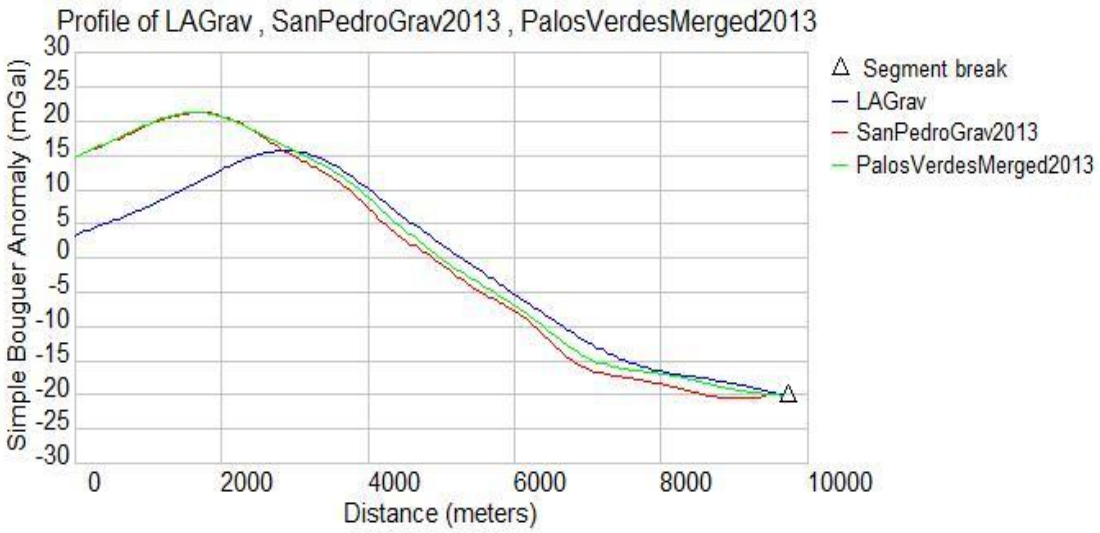

Figure 2.5 The graph along A-A' shows the difference between existing gravity data set and our newly collected gravity data set (The diagram displays at the beginning part of the profile there is 5-10 mGal Bouguer Gravity Anomaly differences between the two data sets)
(LAGrav= the existing gravity data set; SanPedroGrav2013= newly collected gravity data set; PalosVerdesMerged2013= combination of the two data sets).

Although these things above, we had some problems about the integration of our data with pre-existing data. First of all we used EGM96 as a vertical datum but in pre-existing data they used NAVD 88. Of course, it is helpful to relate all position, height, and gravity values of stations to established datum. That ways helps to correlate the ongoing gravity survey with existing works. The used EGM 96 is not exactly same to the NAVD 88 but it is the most close one to NAVD 88. The differences between NAVD88 and EGM 96 at this location are less than 10-20 cm. Secondly, pre-existing data have terrane corrections applied to them, but our data doesn't. The terrain correction finds the variation in the observed gravitational acceleration reasoned by variations in topography in survey area. Therefore when the Simple Bouguer correction is

inadequate to get the aimed answer about gravity surveying, applying terrain correction may be useful. In our survey we did not apply terrain correction because it was not extremely necessary to apply our data set.

Thirdly, when we lead our gravity survey; our observed gravity values were non absolute, they were just measured only with reference to the each other. Therefore we tied our observed gravity anomaly values into a gravity benchmark that in turn tied to the International Gravity Standarization Net. Then absolute gravity values are obtained. Tying observed gravity values to absolute gravity benchmark allowed us to put the context our gravity survey into national or regional data bases. It was absolutely useful to determine the nature of the regional gravity anomaly. These three issues account for the 1-2 mGal difference between our data and pre-existing anomaly values.

In our surveying we calculated the Free-Air and Simple Bouguer Gravity Anomalies.

For computational structural modeling in following chapters we used the values of Simple Bouguer Gravity Anomalies (Appendix B). Ideally, we are left with values, Simple Bouguer Gravity Anomalies that are due to density variations within the subsurface.

CHAPTER 3

STRUCTURAL MODELING

3.1 Introduction

We measured gravity values across the Palos Verdes and Cabrillo faults to obtain more information about the subsurface geology of Palos Verdes Peninsula, Los Angeles. Data of our gravity surveying is properly reduced and have the required accuracy. Also necessary information about rock densities is available and all relevant geologic information is gathered from previous studies.

The next step covered here, is modeling. The modeling process is aimed better determining the geometry of the Palos Verdes and Cabrillo faults. The purpose of the modeling is to provide information about the seismic hazard and the geology of oil producing regimes near the Palos Verdes Peninsula in terms of the location of Palos Verdes and Cabrillo faults.

For modeling we preferred to use GRAVMAG which is a two-dimensional (2-D) gravity modeling program. This kind of 2-D modeling programs reveals gravity anomalies of two-dimensional bodies of varying density that extend infinitely perpendicular to strike. This is a reasonable approximation for geologic scenes in which geology is continuous along strike but fails for more squezed bodies. In GRAVMAG, structural cross-sections based on surface geology and well data were modeled by N-sided polygons and the modeled gravity signature was compared to real gravity observations. Model density values were taken from the density of rocks collected in the field area. On average a 1.0 gr/cm^3 difference was used between the basement and overlying sedimentary rocks. In our survey area the basement rock represented by the Catalina Schist basement rocks and the overlying sedimentary unit is mostly represented by the rocksof Monterey Formation.

The GRAVMAG 2-D modeling program compares calculated anomaly values from the model with observed values from our gravity survey to evaluate the model (Burger et al., 2006). With the program the basic goal is to achieve a best fit between the calculated and observed gravity lines. Initial model geometries were taken from existing geologic observations and drill core data (e.g. Dibblee) and then adjusted until the modeled and observational data match. Density constraints from measured field samples and pinning points from drill cores at the depth to basement are respected in the final model. When a best fit is succeded between lines in the modeling program, it means one possible geologic configuration is at hand.

3.2 Cross-Section Construction

The cross-sections were carefully constructed by using the data presented at Appendix C. All the relevant map sets including topographic and regional gravity maps of the study area were digitized and regulated in Grass GIS program.

3.2.1 Data Preparation

Prior to starting to construct the cross-sections, Simple Bouguer Gravity Anomaly Map of the Palos Verdes Peninsula (constructed by using data from University of El Paso, Texas) was digitized and geo-referenced. The geo-referencing was done by setting up UTM coordinates; UTM easting and UTM northing in Grass GIS program as displayed in data table at Appendix B. The quaternary faults, newly collected gravity station points, and existing gravity station points were located on the Bouguer Gravity Anomaly Maps of the Palos Verdes Peninsula(Figure 3.1). Profile lines were selected along the new jointly gridded gravity map of the Palos Verdes Peninsula. First step was to select profile extensions over new Bouguer Gravity Anomaly Map in Grass GIS, then along these profiles data were extracted.

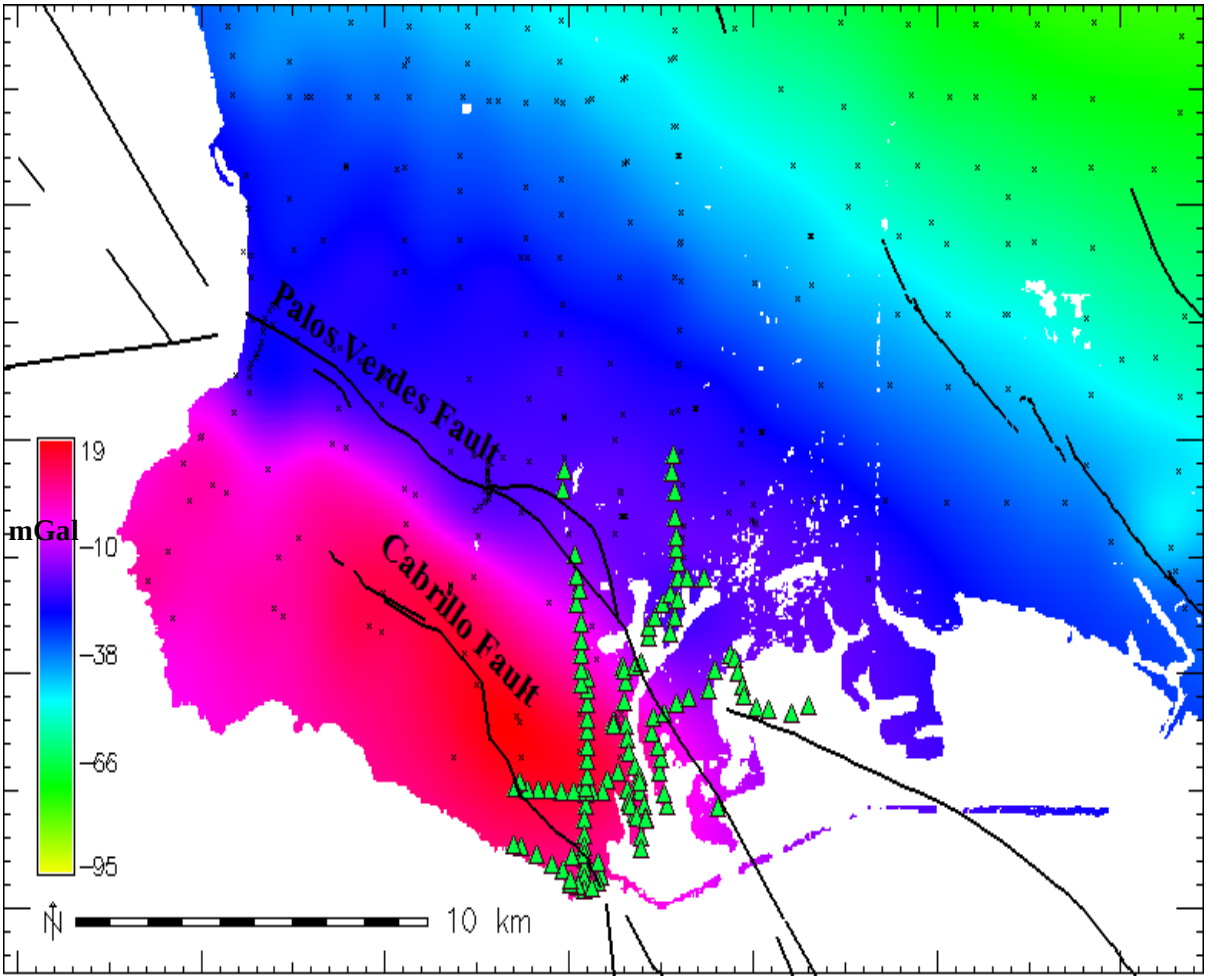

Figure 3.1 Simple Bouguer Gravity Anomaly Map of the Palos Verdes Peninsula showing Quaternary faults (Palos Verdes and Cabrillo faults).(Our measurements indicated by green triangles while previous measurements indicated by black x's).

3.2.2 Orientation of the Cross-Sections

An important component before projecting the data and building structural models, is making decision about the model orientations. In the best of circumstances, the models must be selected to be perpendicular to the fault trends. To determine the 3-D geometry of the Palos Verdes and

Cabrillo faults, we selected 5 different profiles in the orientation from south to north. These different lines are represented on "Geologic Map of Palos Verdes Peninsula and Its Vicinity" drawn by Dibblee, 1999 (Figure 3.2).These lines are not all perfectly perpendicular to the faults, but were selected to maximize data density and the location of a seismic reflection line.

3.2.3 Building the Cross-Sections

The first-step for building cross-sections is to profile selections over Regional Bouguer Gravity Anomaly Maps in the Grass GIS program. Along these profiles, data were exerted as (.csv) file format. Later these files are converted into (.txt) files to import the file in the GRAVMAG 2-D modeling program. The relevant data for the geologic cross-sections were given at Appendix C. After locating the data of different profiles in the GRAVMAG 2-D modeling program, structural geologic cross-sections were constructed.

For all geologic cross-sections the used length is around 10 km and the depth is 3.5 km. As mentioned in previous sections; the GRAVMAG 2-D modeling program uses density anomalies in order to get synchronized, connected cross-sections. The density values of rocks are adjusted to be the same in all models. It is 1.65- 1.75 gr/cm^3 for shallow marine sediments, 1.75 gr/cm^3 for Monterey Formation, and 2.75 gr/cm^3 for Catalina Schist basement rock. Measured density table of collected sample is given at Appendix A.

Overall there is a 30-40 mGal positive Bouguer Gravity Anomaly associated with the Palos Verdes and Cabrillo faults. Our generalized conclusion is that the positive large gravity anomalies are due to the uplift of the Catalina Schist basement rocks. The large gravity anomalies are caused by the uplift of the Catalina Schist basement rocks and the formation of adjacent sedimentary basins in most of the Los Angeles Basin and particularly in terms of the location of the Palos Verdes and Cabrillo faults.

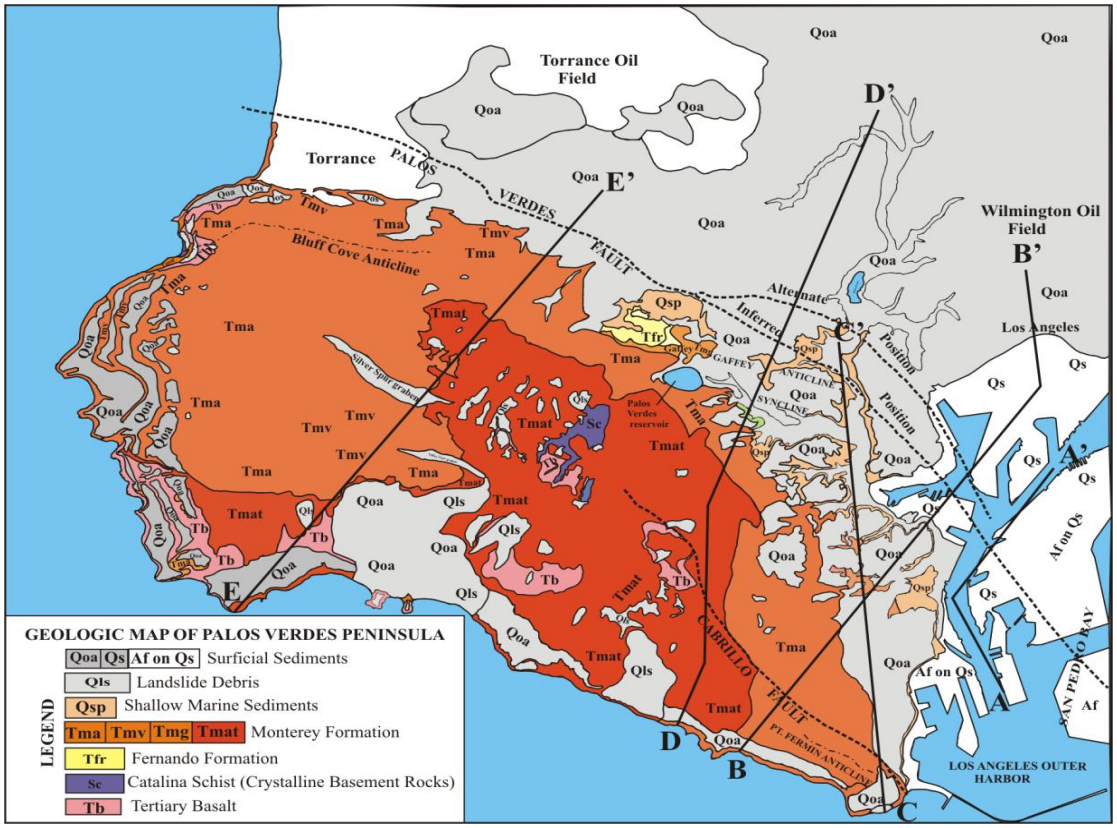

Figure 3.2 Five different profile extensions, (A-A'), (B-B'), (C-C'), (D-D'), (E-E'), on Geologic Map of Palos Verdes Peninsula (modified from "Geologic Map of Palos Verdes Peninsula and Its Vicinity" by Dibblee, 1999).

3.2.3.1 Structural Cross-Section (A-A')

This cross-section is the eastern most of the five and belongs to the line indicated as A-A' in Figure 3.3. This profile runs along Seismic Reflection Line -817 of USGS. It was chosen because combining geophysical applications as seismic and gravity gives a better understanding than one technique alone. The gravity model extends much deeper than seismic reflection profile so the traces of the dipping sediments or vertical faults can be caught better by combining information from gravity surveying and seismic reflection surveying together. In model A-A', at the western

margin of the Palos Verdes fault, the basement rock (Catalina Schist) is covered by rocks of the Monterey Formation. Then Quaternary shallow marine sediments bury rocks of Monterey Formation. When compared with seismic reflection line-817, it may found that in the western part the shallow depths are covered by Quaternary sediments; San Pedro Sand on top and Tims Point siltstone below.

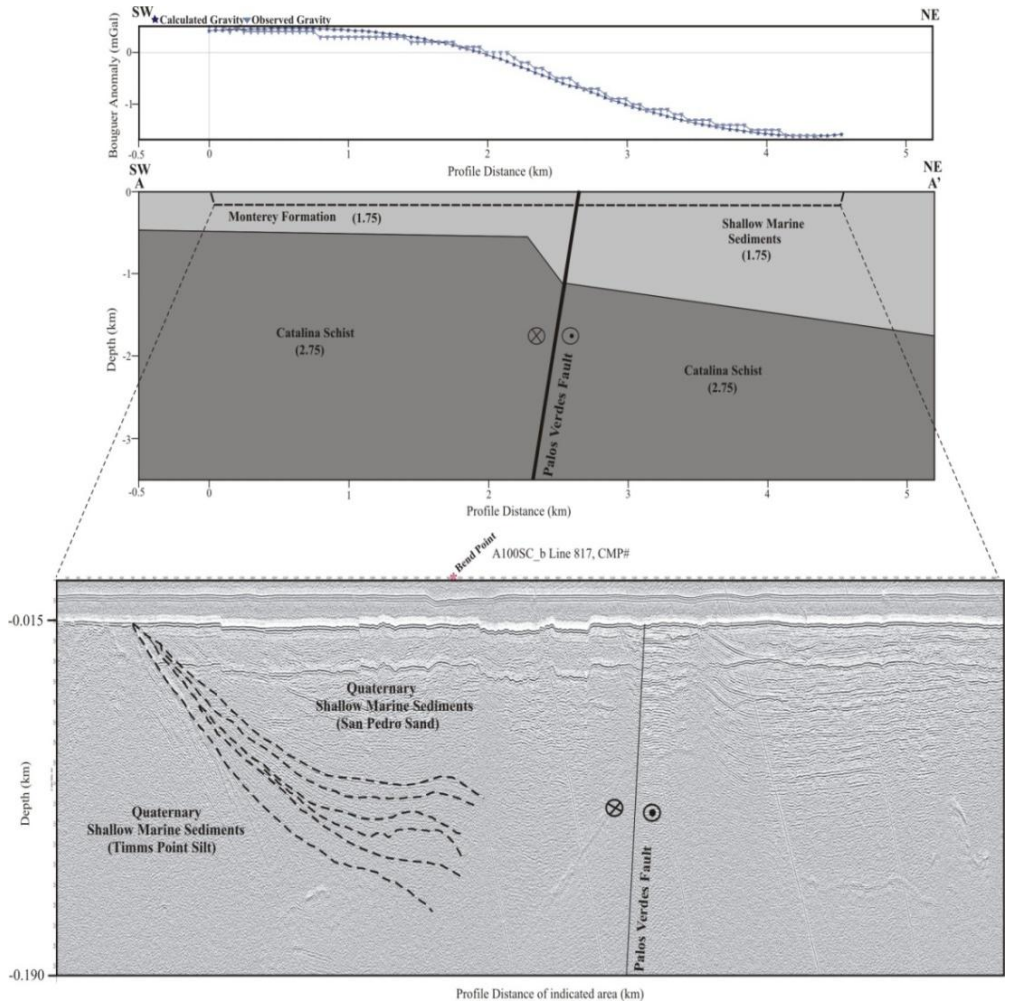

Figure 3.3 Gravity cross-section A-A' (A) and Seismic Reflection Profile of Line-817 of USGS (B). Numbers in parentheses at (A) are density values used in models, in gr/cm^3. Modeling was carried out to a total depth of 3.5 km, and a total width of around 5 km. Depth of seismic profile at (B) is 0.19 km and a total width of 4.7 km and necessary information of A-A' structural cross-section is given at Appendix C-1 (Catalina Schist basement uplift ~0.6 km).

The A-A' profile indicates that the Palos Verdes fault dips to the south with an approximately 80^0. The Monterey Formation rocks next to the fault are folded, but outside of that zone the Catalina Schist basement has been uplifted ~600 m across the Palos Verdes fault in a fault-bend fold type geometry. However, immediately along the PVF, there is little vertical basement offset.

3.2.3.2 Structural Cross-Section (B-B')

This cross-section belongs to the profile B-B' (Figure 3.4). As we move through north at the west of profile A-A', the central part reveals structural discrepancies like folding, anticline, and syncline structures. These deformational structural variations are caused by the changes in stress settings reasoned by the motion between the Cabrillo and Palos Verdes faults.

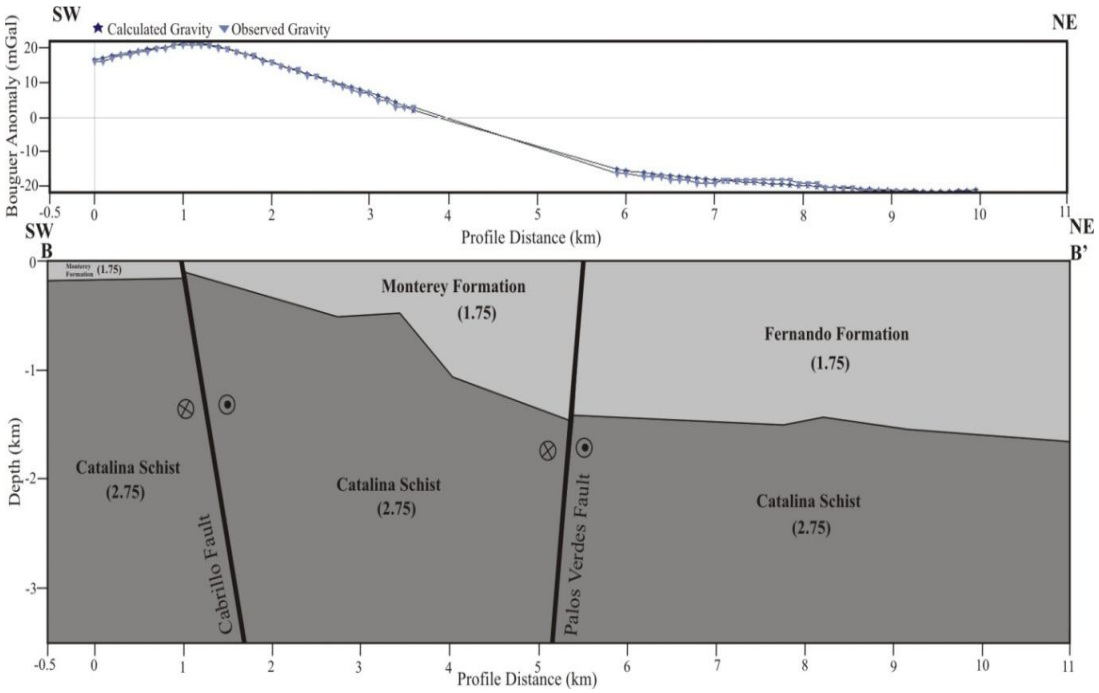

Figure 3.4 Gravity cross-section B-B'. Numbers in parentheses are density values used in models, in gr/cm^3. Modeling was carried out to a total depth of 3.5 km, and a total width of around 11 km and necessary information of B-B' structural cross-section is given at Appendix C-2 (Catalina Schist basement uplift ~1.25 km).

The model B-B' suggests that both Palos Verdes and Cabrillo faults are high angle faults with dips greater than 80^0. The density values of Monterey Formation and Fernando Formation are similar because each units is composed of similar rock types. The dipping histories of faults are similar indicated in both cross-section A-A' and B-B'. Immediately across each fault there is little vertical offset of the Catalina Schist, suggesting little reverse motion. However, between the Palos Verdes and Cabrillo faults the Catalina Schist has been uplifted ~1.25 km. Rotation and folding of the intervening crustal block is needed to explain the uplift.

3.2.3.3 Structural Cross-Section (C-C')

As indicated in previous lines, the model C-C' displays the Cabrillo and Palos Verdes faults dip at high angles > 80^0 (Figure 3.5). While the Cabrillo fault dips to the north, the Palos Verdes fault dips to the south.

There are some small undulations between calculated and observed gravity in gravity along the model C-C' in the central part between the Cabrillo and the Palos Verdes fault. The amplitude of folding increases in this model and the small model misfits may be due to smaller scale folds not included in the model.

The model C-C' shows that neither the Cabrillo fault or Palos Verdes fault seem to have much vertical offset; however, the Cabrillo fault may act as a structural back-step relative to deformations in the central block. North of the Cabrillo fault, the central block is extensively folded and uplifted.

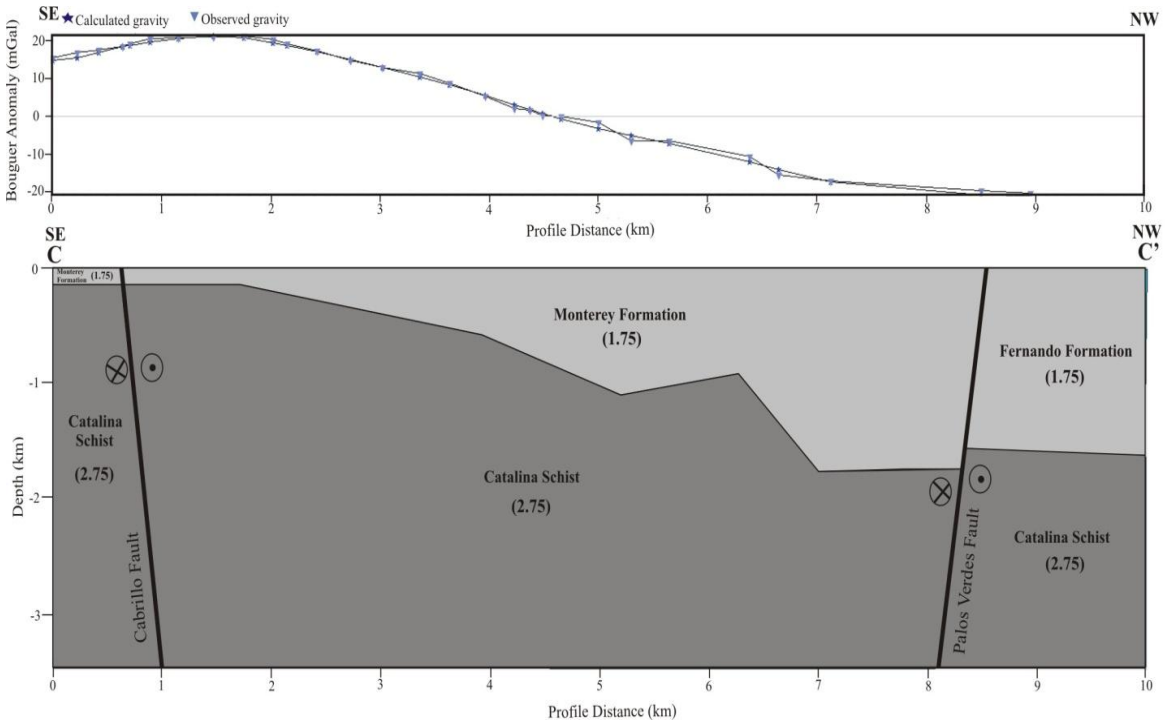

Figure 3.5 Gravity cross-section C-C'. Numbers in parentheses are density values used in models, in gr/cm^3. Modeling was carried out to a total depth of 3.5 km, and a total width of around 10 km and necessary information of C-C' structural cross-section is given at Appendix C-3 (Catalina Schist basement uplift ~1.5 km).

Overall, the Catalina Schist has been uplifted ~1.5 km from the Palos Verdes to the Cabrillo faults. The uplift appears as on B-B' to have been accommodated by block rotation and folding, not fault slip. The greater amount of uplift is interpreted to contribute to the higher amplitude folds.

3.2.3.4 Structural Cross-Section (D-D')

Gravity model D-D' is parallel to the geologic cross section D-D' from Dibblee (1999) (Figure 3.6). Dibblee's D-D' section is constrained by drill cores that we also used. Drill cores used as pinning points are 16,17, and 18. We directly gathered depth information from these drilling points.

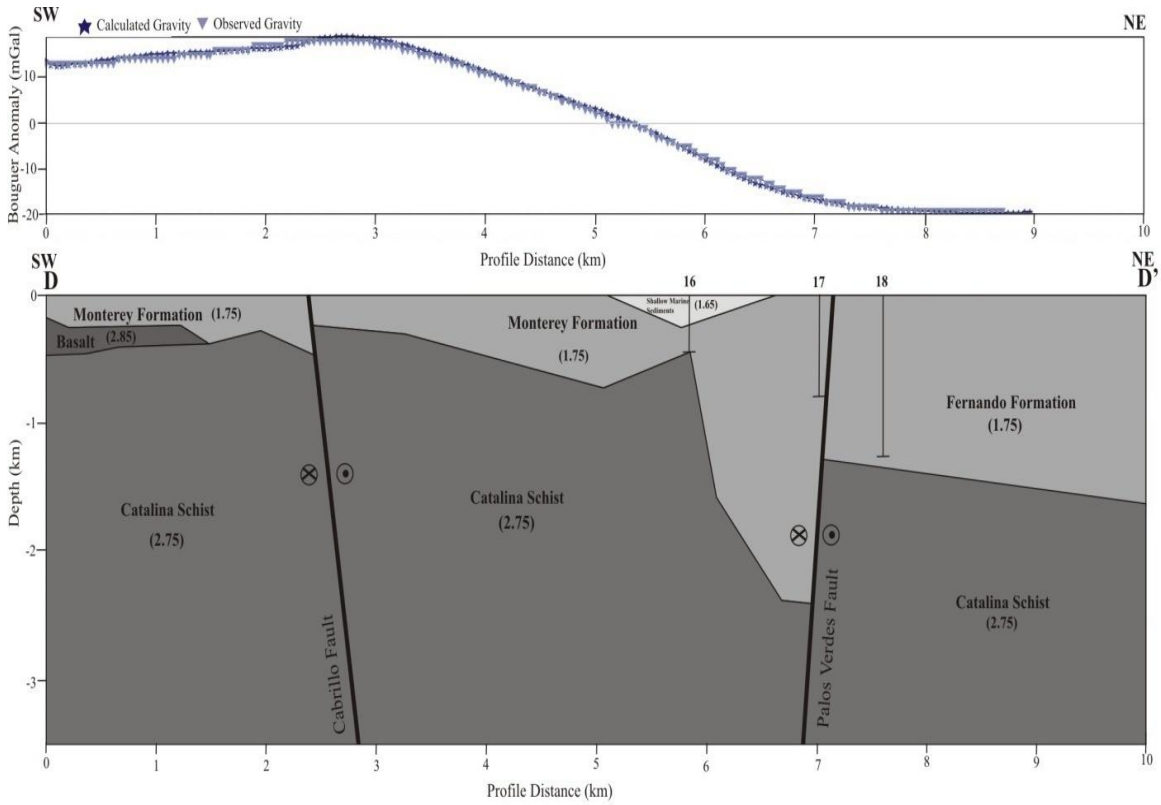

Figure 3.6 Gravity cross-section D-D'. Numbers in parentheses are density values used in models, in gr/cm^3. Modeling was carried out to a total depth of 3.5 km, and a total width of around 10 km and necessary information of D-D' structural cross-section is given at Appendix C-4 (Cataline Schist basement uplift ~1.1 km).

In the model D-D', as given in previous models, the large gravity anomalies are caused by uplift of Catalina Schist basement rocks. Adjacent to the Cabrillo fault the Catalina Schist basement rock is overlain by the Monterey Formation and between these units, there is a high density basalt intrusion. Here this tectonic setting could be explained by some deformational configuration caused by the accumulated strain at this region. Furthermore folding reaches a maximum amplitude in this section and our gravity model requires a greater fold amplitude and geometry than the Dibblee's geologic cross-section. The uplift of the Catalina Schist between the

Cabrillo and Palos Verdes faults is ~1.1 km. This is somewhat less than in sections B-B' and C-C'.

3.2.3.5 Structural Cross-Section (E-E')

Gravity model E-E' on the west side of the Peninsula indicates a southward dip of contact between the Monterey Formation and Catalina Schist north of the Palos Verdes fault (Figure 3.7). This gravity model also indicates a fault- bend fold like geometry, similar to what is observed in profile section A-A'. However, the model also shows a greater amount of Catalina Schist uplift (~1.35 km) than is observed in A-A'.;

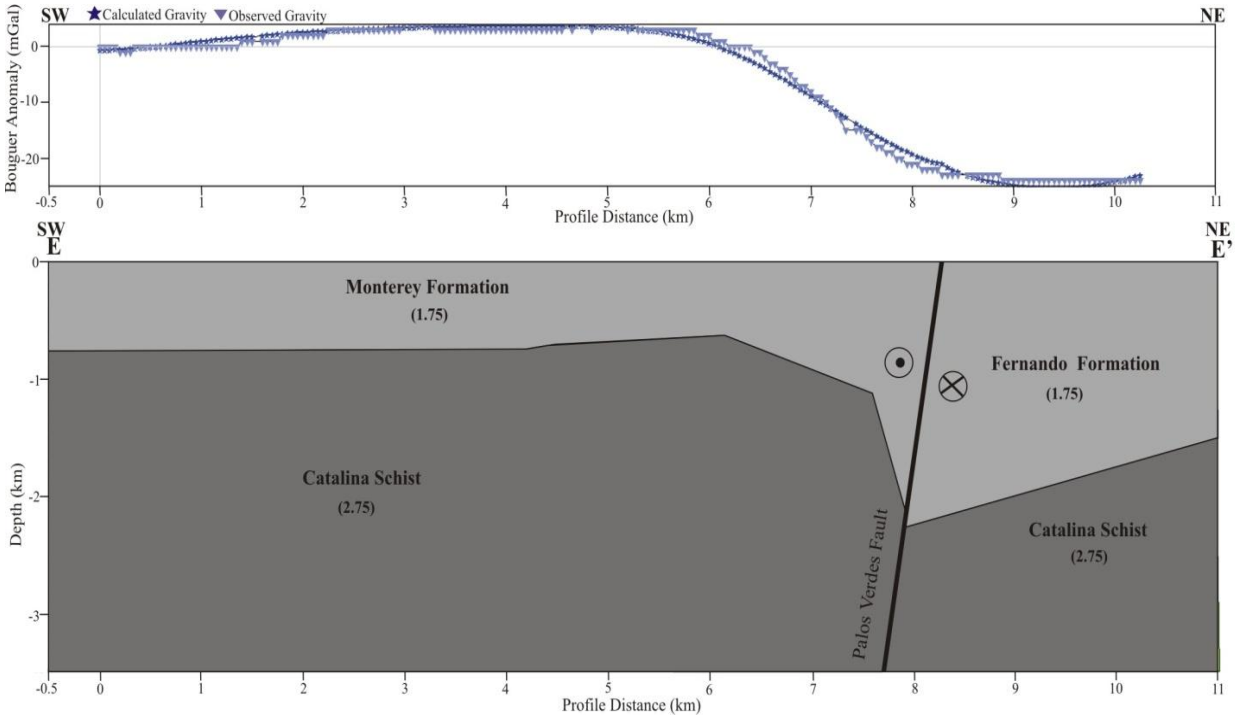

Figure 3.7 Gravity cross-section E-E'. Numbers in parentheses are density values used in models, in gr/cm^3. Modeling was carried out to a total depth of 3.5 km, and a total width of around 10 km and necessary information of E-E' structural cross-section is given at Appendix C-5 (Catalina Schist basement uplift ~1.35 km).

CHAPTER 4

DISCUSSION

The overall goal of this thesis is to better determine the geometry and evolution of the Palos Verdes and Cabrillo faults. It is accomplished some points about these faults. There is a gravity data gap in previously done gravity surveys in San Pedro and Los Angeles Harbor region, particularly in the vicinity of the Cabrillo fault. With our surveying this gap is substantially reduced (Figure 3.1).

By conducting a high-resolution gravity survey in the San Pedro and Los Angeles Harbor region new structural models were constructed to better understand of the Palos Verdes and Cabrillo faults. Newly constructed models were presented in chapter 3. These models clearly indicate the sedimentary succession in the Palos Verdes Peninsula, Los Angeles Basin. As explained in previous chapter by our new constructed models, the basement rocks of the Los Angeles Basin is mostly represented by Catalina Schist basement rocks. The given density value for the Catalina Schist basement rocks unit in literature is 2.75 gr/cm^3. Through much of this rifting the Catalina Schist basement rocks are covered by Miocene Monterey Formation (1.75 gr/cm^3) and younger strata (<1.75 gr/cm^3). This sedimentary succession is clearly exposed on the Palos Verdes Hills as displayed in our structural cross-sections.

In our structural cross-sections (Figure 3.3, Figure 3.4, Figure 3.5, Figure 3.6, Figure 3.7) Simple Bouguer Gravity anomalies are high between the Palos Verdes and Cabrillo faults. Our interpretation for the high-gravity between these two faults is the uplift of the Catalina Schist basement rocks. The Catalina Schist are the crystalline basement rock in the Los Angeles Basin and most of the southern California. When uplifted near the surface, the schist yields high

Bouguer anomaly value. The model in Figure 3.3 shows that dipping beds are representing growth strata deposited during the movement on the PVF. Here down-drop of the Catalina Schist basement rock coupled with extensive Los Angeles Basin low density sedimentary rocks near the Palos Verdes fault which our models also show. This occasion is responsible for the large negative gravity anomalies.

By using high resolution gravity surveying, we seek to identify the geometry of the Palos Verdes fault and adjacent stratigraphic units. In Palos Verdes Peninsula, the style of deformed stratigraphic units indicates that a complex fault geometry dips slightly to the southwest. To understand the earthquake threat posed by Quaternary faults in and near Los Angeles, researchers determined different estimates of slip sense and rate on these faults.

The Palos Verdes fault is one of these faults and first it is thought as a thrust or reverse fault by Namson and Davis (1990) and Shaw and Suppe (1996). Hypocenters 8 to 12 km deep are interpreted to lie along a down-dip, southwestward projection of the PVFZ (Shaw, 1999); the aligned hypocenters show mainly reverse fault movement in this depth range. Other researchers have stated that the PVF has strike-or oblique-slip offset. According to their view, the movement occurs along the PVFZ is mainly strike slip (Nardin and Henyey, 1978; Wright, 1991; Mc Neilan et al., 1996; Bohannon and Geist, 1998). In this view large positive structures along the PVZ have built and they account for the restraining bends in the PVFZ (Fisher et al., 2004).

As pointed in previous chapters the PVF is initially formed as a Miocene normal fault (Woodring et al., 1946). Then Plio-Pleistocene transpression turned it into right lateral reverse fault (Brankman and Shaw, 2009). In previous works the derived slip-rate estimations have been limited to late-Quaternary and Holocene. Most of the expected values comes from paleoseismic studies leaded onshore and in the Los Angeles Outer Harbor (Stephenson et al., 1995; Mc Neilan

et al., 1996). The average slip-rate from these studies is 2.5-3.8 mm/yr. These studies mostly conclude with the PVF is a strike-slip fault.

The gravity models produced here indicate approximately 1-1.5 km of vertical offset across the Cabrillo and Palos Verdes fault system based on offset of the Catalina Schist. Based on slip rate estimations and initiative ages shown below (3.0 mm/yr. of slip since 1.5-3.0 Ma) the Palos Verdes fault has had a total of 5-10 km strike-slip offset. The vertical offset of the Catalina Schist should indicate total offset around 1-1.5 km. Therefore the rate of strike-slip to reverse motion on the PVF system is between 5:1 km and 10:1 km. This indicates that the Palos Verdes fault is pre-dominantly strike-slip fault.

Table 4.1 Slip rate estimates of the PVF depending on different studies by different authors (taken from Brankman and Shaw, 2009).

Study	**Slip rate (mm/yr).**	**Age Range**	**Segment**	**Method**
Ward and Valensise (1994)	3.0-3.7	2.4-3.0 Ma	All	Numerical fault modeling
Stephenson et al. (1995)	2.5-3.8	80-120 k.y.	San Pedro(onshore)	Offset paleochannel
McNeilan et al. (1996)	2.7-3.0	7.8-8.0 k.y.	San Pedro	Offset paleochannel
Rigor (2003)	1.8-5.9	1.6-4.2 Ma	San Pedro	Offset depocenters
	2.6-3.5	3.0-3.6 Ma		offset fault (?)
(strike-slip/uplift rates)	3.4 ± 1.4/3.1 ± 1.5	Active	All	Numerical modeling of Global Positioning System data
Brankman and Shaw (2009)	3.3 ± 0.3/4.0 ±0.3	~ 1.5 Ma	San Pedro Lausen Knoll	Offset basin margins and seismic mapping
	3.3 ±0.3/4.0 ± 0.2			

The Wilmington oil field is located along the southwestern margin of the Los Angeles Basin of southern California. This oil field is one of the most productive oil-producing basins in the world with more than 1.156 billion barrels of oil. The nature of the Wilmington structure consists of asymmetric anticline broken by series of transverse normal faults. These faults around the Wilmington Oil Field divide the producing reservoirs into many separate basins. The oil producing locations age range in age from late to early Miocene. The production is mostly from sandstone beds of varied thickness. Some of the production might be from the blueschist conglomerate immediately above the unconformity in the basin. In our survey, from the beginning it was theorized that the Palos Verdes fault zone is one of the faults bounding structures of the Wilmington Oil Field and includes some of the separated pools. The stratigraphic correlations around the PVF supports this idea.

CHAPTER 5

CONCLUSION

In this study, a high-resolution gravity survey in the San Pedro and Los Angeles Harbor region was used to better determine the 3-D geometry of the Palos Verdes and Cabrillo faults. Approximately 125 new gravity measurements were collected and indicate a large gravity high near the Cabrillo fault that decreases northward towards the Palos Verdes fault. The Palos Verdes fault itself is characterized by an inflection in the gravity data. Modeling of the newly collected data, has yielded five new serial gravity models constructed across the Palos Verdes and Cabrillo faults. The better constrained fault geometry will enhance our understanding of seismic hazard and hydrocarbon bearing structures of the Wilmington Oil Field.

In general our findings;

1. Our observations indicate a large 30-40 mGal Bouguer Gravity anomaly associated with the Cabrillo and Palos Verdes faults in the Palos Verdes Peninsula. This is significantly larger than previous gravity works suggested.

2. The gravity models represented in Chapter 3 suggest that the Cabrillo and the Palos Verdes faults are both high angle faults that have at least a component of reverse motion.

3. The models reveal that the Cabrillo fault dips steeply to the north and the Palos Verdes fault dips steeply to the south. The observed large positive Bouguer Gravity anomaly in models is associated with the uplift of the Catalina Schist basement rocks.

4. Gravity model profiles A-A' through E-E' illustrate the 3-D geometry of the Cabrillo and Palos Verdes faults. Fold amplitude increases towards profile D-D' and decreases away from it.

5. Overall the gravity models display a maximum vertical displacement of the Catalina Schist basement of approximately 1500 meters. From the Los Angeles Harbor region to the center of the Palos Verdes Peninsula uplift of the Catalina Schist progressively increases westward from 600 meters to 1500 meters. However, most of this vertical displacement did not occur as fault slip along either the Palos Verdes and Cabrillo faults, but instead was accommodated by folding and shortening within the intervening block. Maximum fold amplitude and uplift track each other but are not exhibit perfect spatial correlation.

6. Previous workers have estimated the slip rate of the Palos Verdes fault as 2.5-3.8 mm/yr.. This indicates 5-10 km of right-lateral strike-slip displacement over the past 2-3 Ma since fault initiation. Our estimates of vertical uplift of 1.5 km indicate that the ratio of reverse to strike-slip motion at approximately 1:7. Therefore, the Palos Verdes fault itself is primarily a strike-slip fault with only a small component of reverse motion.

APPENDIX A

DENSITY TABLE OF COLLECTED ROCK SAMPLES

Station Name	Description About the Sample	Bedding Strike	Bedding Dip	Dry weight (g)	Submerged weight (g)	Density ($g/cm^{3)}$
13LA113A	pebbly sandstone (Point Fermin)	38	18	506.75	215.6	2.35
13LA113B	black& tan shale/ siltstone			98.2	57.25	1.72
13LA113C	tan limestone cobble			335.5	143.6	2.34
13LA113D	fine grained limestone			352.9	227.4	1.55
13LA127A	massive sandstone (east side Pt Fermin on Gaffey Street)	215	11	203.25	113.95	1.78
13LA127B	siltstone			641.1	333.2	1.92
13LA128A	Bedded and thinly laminated siltstone (Cabrillo Beach, 1-3cm rocks)	84	10	496.25	294.05	1.69
13LA128B	thickly bedded siltstone			398.2	176.9	2.25
13LA128C	siltstone (Cabrillo Beach)			792.4	293.6	2.70
13LA129	sheltered siltstone (near the edge Cabrillo fault& cliffs)	64	14	166.35	96.8	1.72
13LA130A	sandstone (Cabrillo Beach)			483.25	185.35	2.61
13LA130B	siltstone (Cabrillo Beach)			335.25	280.3	1.20
13LA130C	sandstone (Cabrillo Beach)			382.85	154.9	2.47

APPENDIX B

DATA TABLE OF GRAVITY SURVEY

Station Name	WGS 84 Longitude	WGS 84 Latitude	UTM Northing	UTM Easting	WGS 84 GPS Height	EGM 96 GPS Height	Absolute gravity A (mGal)	Absolute gravity B (mGal)	Free-Air Correction	Free-Air Anomaly	Simple Bouguer correction	Simple Bouguer Gravity Anomaly
13LA001	-118.2820	33.7389	3733946.10	381243.84	-2.79	33.64	979624.59		10.38	7.42	3.77	3.65
13LA002	-118.2798	33.7492	3735087.28	381460.25	-32.72	3.66	979621.69		1.13	-5.59	0.41	-6.00
13LA003	-118.2790	33.7463	3734760.85	381535.77	-31.87	4.52	979623.50		1.39	-3.27	0.51	-3.78
13LA003	-118.2790	33.7463	3734760.93	381535.73	-31.83	4.55	979626.75		1.41	-0.01	0.51	-0.52
13LA004	-118.2791	33.7425	3734337.72	381516.97	-31.18	5.23	979630.50		1.61	4.26	0.59	3.68
13LA006	-118.2787	33.7380	3733841.77	381548.61	-33.84	2.58	979631.97		0.80	5.30	0.29	5.01
13LA006B	-118.2784	33.7355	3733563.09	381569.94	-33.16	3.27	979631.97		1.01	5.72	0.37	5.35
13LA006B	-118.2784	33.7355	3733563.05	381569.96	-33.17	3.25	979631.97		1.00	5.71	0.36	5.35
13LA007	-118.2779	33.7326	3733242.52	381612.22	-33.54	2.89	979633.54		0.89	7.40	0.32	7.08
13LA008	-118.2758	33.7301	3732964.70	381810.17	-33.40	3.04	979633.10		0.94	7.22	0.34	6.88
13LA009	-118.2748	33.7283	3732764.86	381895.38	-32.47	3.98	979632.72		1.23	7.29	0.45	6.84
13LA010	-118.2744	33.7254	3732434.09	381931.85	-33.65	2.80	979633.56		0.86	8.01	0.31	7.69
13LA011	-118.2734	33.7227	3732134.41	382022.56	-33.64	2.82	979634.95		0.87	9.63	0.32	9.31
13LA012	-118.2725	33.7202	3731863.42	382100.99	-32.70	3.77	979635.48		1.16	10.66	0.42	10.23
13LA013	-118.2783	33.7255	3732457.29	381574.12	-32.76	3.71	979636.63		1.14	11.34	0.42	10.93
13LA014	-118.2777	33.7234	3732216.83	381624.34	-32.42	4.05	979637.31		1.25	12.31	0.45	11.85
13LA015	-118.2761	33.7212	3731977.90	381769.62	-32.93	3.54	979637.34		1.09	12.36	0.40	11.96
13LA016	-118.2793	33.7488	3735034.25	381507.41	-32.48	3.90	979621.70	979633.76	1.20	-5.47	0.44	-5.91
13LA017	-118.2764	33.7493	3735094.22	381777.94	-32.62	3.75	979619.69	979633.61	1.16	-7.57	0.42	-7.99
13LA018	-118.2745	33.7500	3735163.41	381958.50	-32.98	3.38	979618.20	979633.24	1.04	-9.23	0.38	-9.61
13LA019	-118.2725	33.7550	3735721.41	382149.61	-33.34	2.99	979614.70	979632.85	0.92	-13.27	0.34	-13.61
13LA020	-118.2722	33.7569	3735929.93	382177.38	-33.61	2.71	979613.87	979632.58	0.84	-14.34	0.30	-14.64
13LA021	-118.2707	33.7590	3736162.28	382319.28	-34.36	1.95	979613.05	979631.81	0.60	-15.58	0.22	-15.80
13LA022	-118.2682	33.7614	3736420.88	382549.69	-33.31	2.98	979611.85	979632.84	0.92	-16.66	0.33	-16.99
13LA023	-118.2662	33.7636	3736666.80	382744.80	-33.77	2.50	979611.43	979632.36	0.77	-17.41	0.28	-17.69

Station Name	WGS 84 Longitude	WGS 84 Latitude	UTM Northing	UTM Easting	WGS 84 GPS Height	EGM 96 GPS Height	Absolute gravity A (mGal)	Absolute gravity B (mGal)	Free-Air Correction	Free-Air Anomaly	Simple Bouguer correction	Simple Bouguer Gravity Anomaly
13LA024	-118.2638	33.7664	3736978.17	382969.83	-33.83	2.42	979610.93	979632.29	0.75	-18.17	0.27	-18.44
13LA025	-118.2640	33.7696	3737330.49	382958.00	-32.63	3.61	979610.34	979633.48	1.12	-18.66	0.41	-19.07
13LA026	-118.2643	33.7720	3737589.48	382926.96	-32.59	3.65	979610.12	979633.51	1.13	-19.06	0.41	-19.47
13LA027	-118.2611	33.7667	3736998.59	383219.92	-33.72	2.53	979610.77	979632.39	0.78	-18.32	0.28	-18.60
13LA028	-118.2564	33.7665	3736977.15	383656.54	-33.12	3.11	979610.51	979632.97	0.96	-18.39	0.35	-18.74
13LA029	-118.2640	33.7623	3736517.61	382948.34	-33.90	2.37	979611.34	979632.23	0.73	-17.43	0.27	-17.69
13LA030	-118.2648	33.7588	3736131.73	382868.74	-34.32	1.98	979611.75	979631.84	0.61	-16.85	0.22	-17.07
13LA031	-118.2661	33.7559	3735813.23	382745.14	-33.97	2.33	979613.00	979632.20	0.72	-15.24	0.26	-15.51
13LA032	-118.2645	33.7745	3737868.64	382912.63	-32.58	3.64	979609.73	979633.51	1.12	-19.66	0.41	-20.07
13LA033	-118.2648	33.7783	3738288.14	382890.72	-30.78	5.43	979609.12	979635.29	1.68	-20.04	0.61	-20.65
13LA034	-118.2652	33.7830	3738818.92	382864.96	-27.04	9.15	979607.96	979639.02	2.82	-20.45	1.03	-21.48
13LA035	-118.2662	33.7870	3739255.14	382778.14	-23.92	12.26	979606.95	979642.12	3.78	-20.83	1.37	-22.20
13LA036	-118.2656	33.7904	3739632.67	382834.66	-23.99	12.17	979606.63	979642.03	3.76	-21.46	1.37	-22.82
13LA037	-118.2823	33.7389	3733946.05	381215.87	-21.34	15.09	979630.31	979644.95	4.66	7.41	1.69	5.72
13LA038	-118.2824	33.7380	3733841.31	381202.78	-22.11	14.32	979630.06	979644.19	4.42	7.01	1.61	5.41
13LA039	-118.2664	33.7228	3732142.31	382668.82	-32.03	4.41	979629.07	979634.27	1.36	4.23	0.49	3.73
13LA040	-118.2674	33.7249	3732375.42	382580.37	-32.14	4.30	979629.00	979634.16	1.33	3.94	0.48	3.46
13LA041	-118.2686	33.7293	3732859.91	382471.53	-32.22	4.20	979627.61	979634.07	1.30	2.17	0.47	1.70
13LA042	-118.2684	33.7316	3733114.86	382498.69	-33.28	3.13	979626.32	979632.99	0.96	0.35	0.35	0.00
13LA043	-118.2695	33.7340	3733383.36	382397.99	-33.71	2.70	979625.77	979632.56	0.83	-0.54	0.30	-0.84
13LA044	-118.2711	33.7366	3733677.96	382250.88	-33.25	3.14	979625.32	979633.01	0.97	-1.07	0.35	-1.42
13LA045	-118.2708	33.7395	3733993.34	382284.75	-33.03	3.35	979623.21	979633.22	1.03	-3.35	0.38	-3.73
13LA046	-118.2676	33.7405	3734100.10	382585.66	-33.24	3.13	979620.47	979632.99	0.97	-6.25	0.35	-6.60
13LA047	-118.2641	33.7421	3734283.90	382905.14	-33.15	3.20	979617.50	979633.07	0.99	-9.33	0.36	-9.69
13LA048	-118.2605	33.7436	3734441.08	383243.02	-33.27	3.07	979615.39	979632.93	0.95	-11.60	0.34	-11.95

Station Name	WGS 84 Longitude	WGS 84 Latitude	UTM Northing	UTM Easting	WGS 84 GPS Height	EGM 96 GPS Height	Absolute gravity A (mGal)	Absolute gravity B (mGal)	Free-Air Correction	Free-Air Anomaly	Simple Bouguer correction	Simple Bouguer Gravity Anomaly
13LA050	-118.2529	33.7489	3735014.49	383955.86	-31.43	4.86	979611.87	979634.72	1.50	-15.01	0.55	-15.55
13LA051	-118.2483	33.7519	3735352.24	384382.33	-33.63	2.63	979611.73	979632.50	0.81	-16.09	0.30	-16.39
13LA052	-118.2514	33.7226	3732103.06	384061.54	-31.95	4.44	979618.41	979634.30	1.37	-6.40	0.50	-6.90
13LA053	-118.2470	33.7511	3735258.79	384507.31	-32.34	3.92	979611.03	979633.78	1.21	-16.33	0.44	-16.77
13LA054	-118.2459	33.7485	3734970.53	384604.10	-32.28	3.99	979611.49	979633.85	1.23	-15.64	0.45	-16.08
13LA055	-118.2449	33.7461	3734699.47	384695.30	-32.11	4.16	979611.57	979634.03	1.28	-15.29	0.47	-15.76
13LA056	-118.2440	33.7440	3734469.80	384771.82	-31.88	4.40	979611.81	979634.26	1.36	-14.81	0.49	-15.31
13LA057	-118.2406	33.7419	3734228.11	385081.81	-32.02	4.26	979611.61	979634.12	1.31	-14.87	0.48	-15.35
13LA058	-118.2369	33.7414	3734166.03	385425.39	-32.20	4.07	979611.50	979633.93	1.26	-15.00	0.46	-15.45
13LA059	-118.2303	33.7408	3734093.60	386033.05	-32.30	3.95	979611.29	979633.81	1.22	-15.19	0.44	-15.64
13LA060	-118.2251	33.7424	3734271.69	386520.91	-32.75	3.48	979611.37	979633.34	1.07	-15.40	0.39	-15.79
13LA061	-118.2772	33.7227	3732147.52	381668.81	-32.51	3.97	979637.49	979633.83	1.22	12.52	0.44	12.07
13LA062	-118.2753	33.7203	3731878.79	381836.28	-32.82	3.65	979637.29	979633.51	1.13	12.42	0.41	12.01
13LA063	-118.2740	33.7166	3731459.36	381956.35	-31.83	4.66	979637.21	979634.52	1.44	12.96	0.52	12.44
13LA064	-118.2737	33.7144	3731218.96	381976.36	-31.06	5.43	979636.98	979635.30	1.68	13.15	0.61	12.54
13LA065	-118.2811	33.7289	3732836.71	381312.13	-19.65	16.81	979634.62	979646.68	5.19	13.10	1.89	11.21
13LA066	-118.2838	33.7272	3732653.56	381058.40	-18.90	17.57	979637.79	979647.44	5.42	16.64	1.97	14.67
13LA067	-118.2856	33.7251	3732417.18	380893.82	-17.51	18.98	979640.08	979648.85	5.86	19.55	2.13	17.42
13LA068	-118.2884	33.7252	3732433.95	380637.02	-15.12	21.38	979641.30	979651.24	6.60	21.49	2.40	19.09
13LA069	-118.2903	33.7247	3732379.61	380455.66	-13.12	23.39	979642.25	979653.25	7.22	23.10	2.62	20.48
13LA070	-118.2901	33.7223	3732115.38	380470.49	-8.82	27.70	979642.08	979657.56	8.55	24.46	3.11	21.35
13LA071	-118.2906	33.7199	3731846.45	380422.32	-6.82	29.71	979641.28	979659.57	9.17	24.49	3.33	21.16
13LA071	-118.2906	33.7199	3731846.65	380422.34	-6.83	26.70	979641.28	979656.56	8.24	23.56	2.99	20.56
13LA072	-118.2907	33.7168	3731504.44	380405.81	-7.77	28.77	979640.99	979658.63	8.88	24.16	3.23	20.93

Station Name	WGS 84 Longitude	WGS 84 Latitude	UTM Northing	UTM Easting	WGS 84 GPS Height	EGM 96 GPS Height	Absolute gravity A (mGal)	Absolute gravity B (mGal)	Free-Air Correction	Free-Air Anomaly	Simple Bouguer correction	Simple Bouguer Gravity Anomaly
13LA073	-118.2907	33.7145	3731247.44	380403.46	-7.92	28.63	979640.62	979658.49	8.83	23.94	3.21	20.73
13LA074	-118.2907	33.7121	3730983.25	380401.98	22.94	59.50	979632.18	979689.36	18.36	25.22	6.67	18.55
13LA075	-118.2907	33.7103	3730778.58	380396.37	19.31	55.87	979631.75	979685.73	17.24	23.84	6.27	17.57
13LA076	-118.2907	33.7085	3730583.64	380394.20	6.25	42.82	979633.48	979672.68	13.21	21.68	4.80	16.87
13LA077	-118.2906	33.7064	3730345.03	380400.61	-1.18	35.40	979633.38	979665.26	10.92	19.47	3.97	15.50
13LA078	-118.2906	33.7128	3731065.38	380411.09	11.07	47.62	979635.38	979677.49	14.70	24.71	5.34	19.36
13LA079	-118.2855	33.7090	3730637.37	380881.47	-20.87	15.68	979638.84	979645.54	4.84	18.62	1.76	16.86
13LA080	-118.2866	33.7114	3730897.48	380783.80	-19.16	17.38	979640.12	979647.25	5.36	20.23	1.95	18.28
13LA081	-118.2863	33.7078	3730495.68	380801.65	-3.21	33.35	979634.47	979663.21	10.29	19.81	3.74	16.07
13LA082	-118.2881	33.7068	3730388.80	380637.55	-3.31	33.25	979634.15	979663.12	10.26	19.55	3.73	15.82
13LA083	-118.2924	33.7071	3730426.50	380241.52	1.67	38.25	979633.29	979668.11	11.80	20.20	4.29	15.91
13LA084	-118.2945	33.7073	3730460.06	380044.33	3.74	40.32	979632.52	979670.18	12.44	20.05	4.52	15.53
13LA085	-118.2967	33.7101	3730764.95	379842.52	6.33	42.91	979633.54	979672.77	13.24	21.63	4.81	16.82
13LA086	-118.3002	33.7112	3730889.30	379522.02	3.62	40.21	979633.57	979670.07	12.41	20.74	4.51	16.23
13LA087	-118.3046	33.7127	3731062.36	379111.00	3.25	39.84	979634.21	979669.70	12.29	21.14	4.47	16.68
13LA088	-118.3091	33.7142	3731233.56	378698.62	2.30	38.91	979634.48	979668.77	12.01	21.00	4.36	16.64
13LA089	-118.3112	33.7148	3731301.39	378506.15	1.48	38.08	979634.11	979667.95	11.75	20.33	4.27	16.06
13LA090.	-118.2824	33.7389	3733942.25	381211.12	-21.40	15.03	979630.18	979644.89	4.64	7.28	1.69	5.59
13LA091	-118.2825	33.7379	3733835.90	381199.21	3.27	39.70	979629.99	979669.56	12.25	14.78	4.45	10.32
13LA092	-118.2897	33.7251	3732423.15	380516.74	-13.79	22.71	979641.72	979652.57	7.01	22.33	2.55	19.79
13LA093	-118.2920	33.7251	3732425.64	380300.86	-11.29	25.22	979641.67	979655.09	7.78	23.06	2.83	20.23
13LA094	-118.2941	33.7252	3732442.18	380101.79	7.32	43.83	979637.47	979673.69	13.53	24.59	4.92	19.67
13LA095	-118.2973	33.7251	3732436.38	379805.44	25.57	62.10	979632.66	979691.96	19.16	25.42	6.97	18.45
13LA096	-118.3009	33.7252	3732452.31	379471.36	41.44	77.98	979629.40	979707.84	24.06	27.06	8.75	18.31
13LA097	-118.3044	33.7253	3732460.34	379154.99	50.34	86.88	979627.06	979716.75	26.81	27.46	9.75	17.72

Station Name	WGS 84 Longitude	WGS 84 Latitude	UTM Northing	UTM Easting	WGS 84 GPS Height	EGM 96 GPS Height	Absolute gravity A (mGal)	Absolute gravity B (mGal)	Free-Air Correction	Free-Air Anomaly	Simple Bouguer correction	Simple Bouguer Gravity Anomaly
13LA098	-118.3076	33.7253	3732464.60	378852.84	69.34	105.90	979622.65	979735.76	32.68	28.92	11.88	17.04
13LA099	-118.3096	33.7266	3732614.23	378668.30	76.50	113.06	979620.82	979742.93	34.89	29.18	12.68	16.50
13LA100	-118.3112	33.7255	3732491.07	378525.62	96.07	132.63	979616.27	979762.50	40.93	30.77	14.88	15.89
13LA101	-118.2903	33.7259	3732512.70	380459.33	-13.53	22.97	979641.18	979652.83	7.09	21.81	2.58	19.23
13LA102	-118.2901	33.7283	3732773.29	380478.51	-11.82	24.67	979639.20	979654.53	7.61	20.15	2.77	17.38
13LA103	-118.2901	33.7311	3733092.87	380486.62	-8.66	27.82	979636.33	979657.68	8.59	18.01	3.12	14.89
13LA104	-118.2901	33.7337	3733378.65	380490.85	-6.08	30.39	979634.17	979660.25	9.38	16.43	3.41	13.02
13LA105	-118.2901	33.7368	3733722.98	380493.56	-2.05	34.41	979632.04	979664.27	10.62	15.29	3.86	11.43
13LA106	-118.2900	33.7392	3733988.94	380501.09	-6.44	30.01	979630.56	979659.88	9.26	12.25	3.37	8.88
13LA107	-118.2900	33.7421	3734311.14	380505.45	-8.58	27.86	979627.85	979657.72	8.60	8.63	3.12	5.50
13LA108	-118.2900	33.7447	3734597.77	380510.19	1.52	37.94	979622.73	979667.81	11.71	6.41	4.26	2.15
13LA109	-118.2900	33.7471	3734864.35	380514.46	0.62	37.04	979621.42	979666.90	11.43	4.61	4.15	0.46
13LA110	-118.2824	33.7389	3733941.92	381212.03	-13.75	22.67	979630.21	979652.54	7.00	9.66	2.54	7.12
13LA111	-118.2825	33.7380	3733841.62	381201.75	-22.16	14.27	979629.96	979644.13	4.40	6.90	1.60	5.30
13LA112	-118.2943	33.7124	3731022.91	380068.58	56.62	93.18	979623.91	979723.05	28.76	27.32	10.45	16.87
13LA113	-118.2945	33.7081	3730540.89	380041.57	7.83	44.41	979631.73	979674.27	13.70	20.46	4.98	15.48
13LA114	-118.2728	33.7198	3731821.08	382067.05	-32.50	3.97	979635.22	979633.83	1.22	10.49	0.45	10.04
13LA115	-118.2747	33.7272	3732643.16	381905.10	-33.10	3.35	979633.34	979633.21	1.03	7.80	0.38	7.42
13LA116	-118.2919	33.7460	3734741.30	380334.48	2.74	39.17	979622.26	979669.03	12.09	6.21	4.39	1.81
13LA117	-118.2922	33.7485	3735023.54	380309.85	3.01	39.43	979620.90	979669.29	12.17	4.71	4.42	0.29
13LA118	-118.2922	33.7515	3735353.77	380315.39	0.71	37.12	979619.85	979666.99	11.46	2.70	4.16	-1.46
13LA119	-118.2921	33.7542	3735651.21	380332.78	-32.70	3.70	979621.69	979633.56	1.14	-5.99	0.41	-6.41
13LA120	-118.2921	33.7575	3736023.49	380336.52	-32.56	3.83	979622.12	979633.69	1.18	-5.81	0.43	-6.24
13LA121	-118.2935	33.7611	3736423.73	380213.98	-30.77	5.61	979619.04	979635.47	1.73	-8.64	0.63	-9.27
13LA122	-118.2928	33.7639	3736726.26	380278.25	-27.81	8.55	979614.80	979638.41	2.64	-12.20	0.96	-13.16

Station Name	WGS 84 Longitude	WGS 84 Latitude	UTM Northing	UTM Easting	WGS 84 GPS Height	EGM 96 GPS Height	Absolute gravity A (mGal)	Absolute gravity B (mGal)	Free-Air Correction	Free-Air Anomaly	Simple Bouguer correction	Simple Bouguer Gravity Anomaly
13LA123	-118.2936	33.7665	3737021.06	380205.04	-27.36	9.00	979612.89	979638.86	2.78	-14.19	1.01	-15.20
13LA124	-118.2941	33.7706	3737477.13	380166.78	-28.12	8.22	979611.68	979638.09	2.54	-15.98	0.92	-16.90
13LA125A	-118.2978	33.7829	3738844.76	379844.97	-16.92	19.39	979607.96	979649.25	5.98	-17.28	2.17	-19.45
13LA126.	-118.2974	33.7870	3739299.36	379890.04	-21.46	14.82	979608.55	979644.68	4.57	-18.44	1.66	-20.10

APPENDIX C

MODEL PARAMETERS IN GRAVITY MODELS

C.1 Model Parameters of Structural Cross-Section A-A'

LeftEdge,-500

RightEdge,5200

Bottom,3500

ProfileAzimuth,0

Latitude,40

Body,1,-0.7,0.001,6,0.0001,0,1.033414

X,-0.5,Z,-0.0151844

X,0.9744898,Z,-0.0151844

X,2.645578,Z,-0.0075922

X,2.547755,Z,-1.146421

X,2.289864,Z,-0.5542299

X,-0.4942177,Z,-0.4479393

Color,52,229,22

Body,2,-0.7,0.001,6,0.0001,0,1.033414

X,2.57102,Z,-1.10846

X,2.657551,Z,-0.0227766

X,5.186463,Z,-0.0303688

X,5.176735,Z,-0.8579176

X,5.180612,Z,-1.746204

X,4.556327,Z,-1.586768

Color,22,81,229

Body,3,0.3,0.001,5,0.0001,0,1.033414

X,-0.4826531,Z,-0.478308

X,2.280204,Z,-0.5845987

X,2.54,Z,-1.17679

X,2.315986,Z,-3.462039

X,-0.4710884,Z,-3.477223

Color,229,22,111

Body,4,0.3,0.001,6,0.0001,0,1.033414

X,4.676531,Z,-1.647505

X,5.188367,Z,-1.761388

X,5.18449,Z,-2.70282

X,5.176735,Z,-3.462039

X,2.336599,Z,-3.454447

X,2.559388,Z,-1.123644

Color,140,229,22

C.2 Model Parameters of Structural Cross-Section B-B'

LeftEdge,-500

RightEdge,11000

Bottom,3500

ProfileAzimuth,0

Latitude,40

Body,2,0.3,0.001,4,0.0001,0,1.033414

X,-482.362,Z,-188.172

X,1025.69,Z,-169.3548

X,1644.885,Z,-3467.814

X,-485.0466,Z,-3490.591

Color,22,81,229

Body,3,-0.7,0.001,4,0.0001,0,1.033414

X,-500,Z,-9.408602

X,997.6994,Z,-9.408602

X,1025.69,Z,-141.129

X,-488.1135,Z,-178.7634

Color,229,22,111

Body,4,-0.7,0.001,11,0.0001,0,1.033414

X,1002.041,Z,-22.77657

X,2945.143,Z,-13.36797

X,4157.566,Z,-13.36797

X,5518.763,Z,-13.36797

X,5416.385,Z,-822.5078

X,5367.347,Z,-1457.701

X,4049.438,Z,-1067.131

X,3440.925,Z,-483.7981

X,2735.404,Z,-512.0239

X,1650.665,Z,-220.3572

X,1050.971,Z,-98.04539

Color,140,229,22

Body,5,0.3,0.001,9,0.0001,0,1.033414

X,1034.509,Z,-94.08602

X,1581.288,Z,-206.9892

X,2736.58,Z,-526.8817

X,3433.282,Z,-489.2473

X,4032.975,Z,-1081.989

X,5367.347,Z,-1472.885

X,5241.181,Z,-2483.871

X,5144.172,Z,-3481.183

X,1676.579,Z,-3479.041

Color,22,170,229

Body,6,-0.7,0.001,8,0.0001,0,1.033414

X,5523.81,Z,7.592191

X,10965.14,Z,-1.816411

X,10965.33,Z,-103.362

X,10968.13,Z,-1634.137

X,9082.757,Z,-1527.847

X,8199.32,Z,-1419.74

X,7753.401,Z,-1480.477

X,5390.24,Z,-1398.78

Color,229,22,199

Body,7,0.3,0.001,7,0.0001,0,1.033414

X,5398.639,Z,-1404.555

X,7753.401,Z,-1503.254

X,8222.789,Z,-1434.924

X,9318.027,Z,-1563.991

X,10984.35,Z,-1655.098

X,10973.25,Z,-3466.203

X,5179.543,Z,-3485.02

Color,228,229,22

C.3 Model Parameters of Structural Cross-Section C-C'

LeftEdge,0

RightEdge,10000

Bottom,3500

ProfileAzimuth,0

Latitude,40

Body,1,0.3,0.001,4,0.0001,0,1.033414

X,0,Z,-159.436

X,659.8639,Z,-167.0282

X,1027.211,Z,-3462.039

X,13.60544,Z,-3462.039

Color,52,229,22

Body,2,-0.7,0.001,4,0.0001,0,1.033414

X,6.802721,Z,-15.18438

X,619.0476,Z,-15.18438

X,639.4558,Z,-159.436

X,6.802721,Z,-144.2516

Color,22,81,229

Body,3,-0.7,0.001,10,0.0001,0,1.033414

X,639.4558,Z,-15.18438

X,8530.613,Z,-30.36876

X,8292.517,Z,-1715.835

X,7857.143,Z,-1753.796

X,7000,Z,-1776.573

X,6258.504,Z,-895.8785

X,5183.674,Z,-1100.868

X,3904.762,Z,-592.1909

X,1680.272,Z,-144.2516

X,646.2585,Z,-151.8438

Color,229,22,111

Body,4,0.3,0.001,11,0.0001,0,1.033414

X,2721.088,Z,-364.4252

X,3911.565,Z,-592.1909

X,5170.068,Z,-1116.052

X,6258.503,Z,-926.2473

X,7013.605,Z,-1806.941

X,7850.34,Z,-1776.573

X,8292.517,Z,-1738.612

X,8061.224,Z,-3484.815

X,1020.408,Z,-3477.223

X,659.8643,Z,-151.8438

X,1687.075,Z,-151.8438

Color,140,229,22

Body,5,-0.7,0.001,4,0.0001,0,1.033414

X,8551.02,Z,-15.18438

X,10000,Z,-15.18438

X,9972.789,Z,-1617.137

X,8326.531,Z,-1579.176

Color,22,170,229

Body,6,0.3,0.001,4,0.0001,0,1.033414

X,8326.531,Z,-1586.768

X,9986.395,Z,-1647.505

X,9986.394,Z,-3467.101

X,8088.435,Z,-3469.631

Color,229,22,199

C.4 Model Parameters of Structural Cross-Section D-D'

LeftEdge,0

RightEdge,10000

Bottom,3500

ProfileAzimuth,0

Latitude,40

Body,1,-0.7,0.001,8,0.0001,0,1.033414

X,6.802721,Z,-7.592191

X,2387.755,Z,-7.592191

X,2455.782,Z,-455.5315

X,1972.789,Z,-288.5033

X,1523.81,Z,-364.4252

X,1312.925,Z,-303.6876

X,190.4762,Z,-250.5423

X,20.40816,Z,-182.2126

Color,52,229,22

Body,2,0.3,0.001,9,0.0001,0,1.033414

X,0,Z,-463.1236

X,272.1088,Z,-455.5315

X,741.4966,Z,-379.6095

X,1496.599,Z,-394.7939

X,1965.986,Z,-303.6876

X,2448.98,Z,-470.7158

X,2653.061,Z,-2008.134

X,2836.735,Z,-3484.815

X,0,Z,-3484.816

Color,22,81,229

Body,3,-0.7,0.001,13,0.0001,0,1.033414

X,2408.163,Z,-15.18438

X,5088.435,Z,-22.77657

X,5761.905,Z,-250.5423

X,6673.469,Z,-22.77657

X,7183.674,Z,-22.77658

X,7074.83,Z,-1199.566

X,6979.592,Z,-2406.725

X,6693.878,Z,-2376.356

X,6102.041,Z,-1601.952

X,5859.706,Z,-427.348

X,5102.041,Z,-706.0738

X,3258.503,Z,-273.3189

X,2435.374,Z,-189.8048

Color,229,22,111

Body,4,0.3,0.001,9,0.0001,0,1.033414

X,2428.571,Z,-197.397

X,3258.503,Z,-296.0954

X,5102.041,Z,-713.6659

X,5836.735,Z,-432.7549

X,6081.633,Z,-1571.584

X,6687.075,Z,-2383.948

X,6979.592,Z,-2421.909

X,6884.354,Z,-3477.223

X,2836.735,Z,-3477.223

Color,255,128,0

Body,5,-0.7,0.001,4,0.0001,0,1.033414

X,7176.871,Z,-22.77657

X,9970.809,Z,-17.36973

X,9979.592,Z,-1647.505

X,7081.633,Z,-1298.265

Color,22,170,229

Body,6,0.3,0.001,4,0.0001,0,1.033414

X,7081.633,Z,-1313.449

X,9965.986,Z,-1670.282

X,9972.789,Z,-3462.039

X,6897.959,Z,-3469.631

Color,229,22,199

Body,7,-0.8,0.001,4,0.0001,0,1.033414

X,5761.905,Z,-15.18438

X,6646.259,Z,-15.18438

X,5761.905,Z,-242.9501

X,5081.633,Z,-22.77657

Color,228,229,22

Body,8,0.4,0.001,8,0.0001,0,1.033414

X,20.40816,Z,-447.9393

X,20.40816,Z,-197.3969

X,183.6735,Z,-265.7267

X,482.9932,Z,-280.9111

X,1299.32,Z,-311.2798

X,1510.204,Z,-379.6095

X,734.6939,Z,-356.833

X,238.0952,Z,-447.9393

Color,22,229,200

C.5 Model Parameters of Structural Cross-Section E-E'

LeftEdge,-500

RightEdge,11000

Bottom,3500

ProfileAzimuth,0

Latitude,40

Body,1,-0.7,0.001,8,0.0001,0,1.033414

X,2183.333,Z,-22.77657

X,8281.972,Z,-15.18438

X,7930.272,Z,-2148.59

X,7596.939,Z,-1108.46

X,6134.353,Z,-614.9675

X,3996.599,Z,-751.6269

X,-486.0544,Z,-774.4035

X,-493.8775,Z,-15.18438

Color,52,229,22

Body,2,0.3,0.001,7,0.0001,0,1.033414

X,-476.5306,Z,-789.5879

X,4076.531,Z,-759.2191

X,6131.292,Z,-614.9675

X,7573.469,Z,-1100.868

X,7912.245,Z,-2125.813

X,7680.272,Z,-3484.815

X,-492.1769,Z,-3469.631

Color,22,81,229

Body,3,-0.7,0.001,4,0.0001,0,1.033414

X,8306.122,Z,-15.18438

X,10970.07,Z,-15.18438

X,10992.18,Z,-1503.254

X,7902.041,Z,-2277.657

Color,229,22,111

Body,4,0.3,0.001,4,0.0001,0,1.033414

X,7909.864,Z,-2308.026

X,10968.71,Z,-1526.03

X,11007.82,Z,-3477.223

X,7698.639,Z,-3462.039

Color,140,229,22

REFERENCES CITED

Argus, D. F., Heflin, M. D., Donnellan, A., Webb, F. H., Dong, D., Hurst, K. J., Jefferson, D. C., Lyzenga, G. A., Watkins, M. M., and Zumberge, J. F., 1999, Shortening and thickening of metropolitan Los Angeles measured and inferred by using geodesy, *Geology 27,* pp. 703-706.

Baher, S., Fuis, G., Sliter, R., and Normark, W. R., 2005, Upper-crustal structure of the inner continental borderland near Long Beach, California, *Bulletin of the Seismological Society of America*, vol. 95; No. 5; pp. 1957- 1969.

Bilodeau, W.L., Bilodeau, S.W., Gath, E.M., Oborne, M., and Proctor, R.J., 2007, Geology of Los Angeles, California, United States of America, Association of Environmental and Engineering Geologists and Geological Society of America, *Environmental & Engineering Geoscience Bulletin*. vol. 13; No. 2; pp. 99-160.

Bohannon, R. G., and Geist, E., 1998, Upper crustal structure and Neogene tectonic development of the California continental borderland, *GSA Bulletin*, vol. 110; No. 68; pp. 779-800.

Brankman, C. M., and Shaw, J. H., 2009, Structural geometry and slip of the Palos Verdes fault, Southern California: Implications for earthquake hazards, *Bulletin of the Seismologic Society of America*, vol. 99; No. 3; pp. 1730-1745.

Bryant, M. E., and Raub, M. L., 1986, The Cabrillo fault-A Structural Problem: *Geology and landslides of the Palos Verdes Hills*, pp. 64-68.

Burger, H. R., Sheehan, A. F., and Jones, C. H., 2006, Introduction to Applied Geophysics: Exploring the shallow subsurface, *W.W. Norton & Company*, in chapter 6; pp. 349.

Clarke, S. H., Green, H. G., and Kennedy, M. P., 1985, Identifying potentially active faults and unstable slopes offshore, in *Evaluating earthquake hazards in the Los Angeles region-an earth-science perspective*, Ziony, J.I. (Editor), *U.S. Geol. Surv.* Prof. Paper, No. 1360; pp. 347- 374.

Conrad, C. L. and Ehlig, P. L., 1987, The Monterey Formation of the Palos Verdes Peninsula, California: an example of sedimentation in a tectonically active basin with the California continental borderland: Geology of the Palos Verdes Peninsula and San Pedro Bay, in Fisher, P. J. (Editor), *Society of Economic Paleontologists and Mineralogists, United States,* vol. *55*; pp. 17-30.

Cooke, M. L., and Marshall, S. T., 2006, Fault slips rates from three-dimensional models of the Los Angeles metropolitan area, California, *Geophys. Res. Lett.*, No. 33; pp. L21313.

Crouch, J. K., and Suppe, J., 1993, Neogene tectonic evolution of the Los Angeles basin and inner borderland: A model for core complex-like crustal extension: *Geological Society of America Bulletin*, vol. 105; pp. 1415-1434.

Darrow, A. C., and Fischer, P. J., 1983, Final Technical Report, Activity and Earthquake Potential of the Palos Verdes fault Zone, published jointly by Damed &Moore, Los Angeles, California and Marine Environmental Science Associates ($MESA^2$), Northridge, California, USGS contact No:14-08-0001-19786.

Diblee, T. W., Ehrenspect, H. E., Ehlig, P. L., and Barlett, W. L., 1999, Geologic map of the Palos Verdes Peninsula and vicinity, Redondo Beach, Torrance, and San Pedro quadrangles, Los Angeles County, California; Dibblee Foundatin Map DF-70.

Dickinson, W.R., 1996, Kinematics of transrotational tectonism in the California Transverse Ranges and its contribution to cumulative slip along the San Andreas transform fault; *Geological of America Special Paper*, No. 305; pp. 50.

Fischer, P. J., Patterson, R. H., Darrow, A. C., Rudat, J. H., and Simila, G., 1987, The Palos Verdes fault zone: Onshore to offshore, *in Geology of the Palos Verdes Peninsula and San Pedro Bay, SEPM Guidebook*, Fischer P.J. (Editor), Society of Economic Paleontologists and Mineralogists, American Association of Petroleum Geologists, Los Angeles, California, No.91; pp. 133.

Fisher, M. A., Normark, W. R., Langenheim, V. E., Calvert, A .J., and Sliter, R., 2004, The offshore Palos Verdes fault zone near San Pedro, southern California, *Bull. Seismol. Soc. Am. 94*, No. 2; pp. 506–530.

Ingersoll, R. V., 2001, Tectonostratigraphy of the Santa Monica Mountains, southern California. In Wright, T. L. and Yeats, R. S. (Editors), *Geology and Tectonics of the San Fernando Valley and East Venture Basin, Calirfornia*: Pacific Section, American Association of Petroleum Geologists, Guidebook GB 77, Los Angeles, CA, pp. 63-70.

International Gravity Standarization Net, 1971, *Bulletin of Geodesy*, Springer- Verlag, doi.org/10.1007/BF02521481.

Jennings, C. W., 1994, Fault activity map of California and adjacent areas, California Department of Conservation, Division of Mines and Geology, Geologic Data Map No. 6, scale 1:750,000.

Larson, A. A., 2000, Defining the fault that caused the 1979 and 1989 Malibu earthquakes in Santa Monica Bay, *California, A.B Thesis,* Harvard University, pp. 66.

McNeilan, T. W., Rockwell, T. K., and Resnick, G. S., 1996, Style and rate of Holocene slip, Palos Verdes fault, southern California, *J. Geophys. Res.*, No. 101; pp. 8317–8334.

Meade, B. J., and Hager, B. H., 2005, Block models of crustal motion in southern California constrained by GPS measurements, *J. Geophys. Res.*, No. 110; pp. B03403.

Namson, J. S., and Davis, T. L., 1990, Late Cenozoic fold and thrust belt of the southern Coast Ranges and Santa Maria basin, California: *American Association of Petroleum Geologists Bulletin,* vol. 74; pp. 467-492.

Robinson, E. S., Coruh, C., 1988, *Basic exploration geophysics,* By John Wiley and Sons, Inc. ISBN 0-471-87941-X.

Rowell, H. C., 1982, Chronostratigraphy of the Monterey Formation of the Palos Verdes Hills; Landslides and landslide abatement, Palos Verdes Peninsula, Southern California, *Host Book: Assoc. Eng. Geol., Southern California Section., California,* Field trip No.10, pp. 7-13.

Shaw, J. H., and Shearer, P. M., 1999, Earthquake hazards of active blind-thrust faults under the central Los Angeles Basin, California: *Journal Geophysical Research,* vol. 101; pp. 8623-8642.

Shaw, J. H., and Suppe, J., 1996, Earthquake hazards of active blind-thrust faults under the central Los Angeles Basin, California, *Journal of Geophysical Research, B, Solid Earth and Planets,* vol. 101, No. 4, pp. 8623-8642.

Sorlien, C. C., Kamerling, M. J., Seeber, L., and Broderick, K. G., 2006, Restraining segments and reactivation of the Santa Monica-Dume-Malibu Coast fault system, offshore Los Angeles, California, *J. Geophys. Res*., No. 111, B11402.

Stephenson, W. J., Rockwell, T. K., Odum, J. K., Shedlock, K. M., and Okaya, D. A., 1995, Seismic reflection and geomorphic characterization of the onshore Palos Verdes fault zone, Los Angeles, California, *Bull. Seismol. Soc. Am*. 85, No. 3; pp. 943–950.

United States Geological Survey, Menlo Park, California, 2000, chief scientists; Gutmacher, C., Ross, S., Edwards, B., Geophysical data of field activity A-1-00-SC, Seismic_Line-817 in southern California.

Wallace, R. E., 1990, The San Andreas fault System, California, *Geological Survey (U.S). USGS Numbered Series,* No. 1515; pp. 283.

Walls, C., Rockwell, T., Mueller, K., Bock, Y., Williams S., Pfanner, J., Dolan, J., and Feng, P., 1998, Escape tectonics in the Los Angeles metropolitan region and implications for seismic risk, *Nature,* No. 394; pp. 356–360.

Ward, S. N., and Valensise, G., 1994, The Palos Verdes terraces, California: Bathtub rings from a buried reverse fault, *J. Geophys. Res*., No. 99; pp. 4485–4494.

Woodring, W. P., Bramlette, M. N., and Kew, W. W. S., 1946, Geology of the Palos Verdes Peninsula: *U.S. Geological Survey Professional Paper,* No.207, pp. 145.

Wright, T. L., 1991, Structural geology and tectonic evolution of the Los Angeles Basin, California, in *Active Margin Basins,* K. T. Biddle (Editor), Am. Assoc. Pet. Geol. Memoir , No. 52, pp. 35–134.

BIOGRAPHICAL SKETCH

Yeliz Cengelcik

Yeliz Cengelcik was born in Zonguldak, Turkey on the 11th of January, 1988. She is graduated from 75. Yil Karabuk Anatolian High School in 2006, and received a Bachelor's of Sciences in Geophysical Engineering from Suleyman Demirel University in the Spring 2010. During the college years in T.C Suleyman Demirel University she was awarded to be a representative of the Department of Geophysical Engineering. When she got her bachelor degree, she achieved a full sponsorship for Graduate Education in the US, and sponsored by both the Ministry of Education of Turkey and Turkish Petroleum Corporation (TPAO). She got admitted by Earth, Ocean, and Atmospheric Sciences Department of Geology at Florida State University in the Fall 2012. She contributed her graduate research under the guidance of Dr. David Farris. She completed her Master's degree in the Fall 2014.